JGR Space Physics

RESEARCH ARTICLE
10.1029/2023JA031359

Special Section:
Understanding the interconnected sun-heliospheric-planetary system during solar minimum

Prediction and Verification of Parker Solar Probe Solar Wind Sources at 13.3 $R_\odot$

S. T. Badman[1], P. Riley[2], S. I. Jones[3,4], T. K. Kim[5], R. C. Allen[6], C. N. Arge[4], S. D. Bale[7,8], C. J. Henney[9], J. C. Kasper[10], P. Mostafavi[6], N. V. Pogorelov[5], N. E. Raouafi[6], M. L. Stevens[2], and J. L. Verniero[3]

[1]Center for Astrophysics | Harvard & Smithsonian, Cambridge, MA, USA, [2]Predictive Science Inc., San Diego, CA, USA, [3]NASA Goddard Space Flight Center, Greenbelt, MD, USA, [4]Catholic University of America, Washington, DC, USA, [5]University of Alabama, Huntsville, AL, USA, [6]The Johns Hopkins Applied Physics Lab, Laurel, MD, USA, [7]Physics Department, University of California, Berkeley, CA, USA, [8]Space Sciences Laboratory, University of California, Berkeley, CA, USA, [9]Air Force Research Laboratory, Space Vehicles Directorate, Kirtland AFB, NM, USA, [10]BWX Technologies Inc., Washington, DC, USA

Abstract Drawing connections between heliospheric spacecraft and solar wind sources is a vital step in understanding the evolution of the solar corona into the solar wind and contextualizing in situ timeseries. Furthermore, making advanced predictions of this linkage for ongoing heliospheric missions, such as Parker Solar Probe (Parker), is necessary for achieving useful coordinated remote observations and maximizing scientific return. The general procedure for estimating such connectivity is straightforward (i.e., magnetic field line tracing in a coronal model) but validating the resulting estimates is difficult due to the lack of an independent ground truth and limited model constraints. In its most recent orbits, Parker has reached perihelia of 13.3$R_\odot$ and moreover travels extremely fast prograde relative to the solar surface, covering over 120° longitude in 3 days. Here we present footpoint predictions and subsequent validation efforts for Parker Encounter 10, the first of the 13.3$R_\odot$ orbits, which occurred in November 2021. We show that the longitudinal dependence of in situ plasma data from these novel orbits provides a powerful method of footpoint validation. With reference to other encounters, we also illustrate that the conditions under which source mapping is most accurate for near-ecliptic spacecraft (such as Parker) occur when solar activity is low, but also require that the heliospheric current sheet is strongly warped by mid-latitude or equatorial coronal holes. Lastly, we comment on the large-scale coronal structure implied by the Encounter 10 mapping, highlighting an empirical equatorial cut of the Alfvèn surface consisting of localized protrusions above unipolar magnetic separatrices.

Plain Language Summary Parker Solar Probe (Parker) is a NASA heliospheric mission which travels closer to the Sun than any previous human-made object, but also is the first to fly faster than the Sun rotates and so skims over its surface in a new way. To get the most out of Parker's science and to tie its measurements of the solar wind back to the physics happening at the Sun, we need to estimate the solar origin of the plasma which later arrives at Parker. This paper describes how we predict these locations in advance of seeing the Parker data as well as how we check how well we did after the fact. We show how Parker's extremely fast motion across the Sun in recent orbits leads to new and powerful ways to verify our estimates. We show the conditions which make our predictions the most accurate is when there is low solar activity, but plenty of "equatorial coronal holes": dark regions seen near the Sun's equator where the Sun's plasma is able to escape into space. Lastly, we show how the connectivity exercise combined with the novel Parker orbital motion allows us to "measure" a large portion of the Sun's atmosphere and relate these measurements to how the magnetic field lines of the Sun are arranged closer to the solar surface.

Key Points:

- Parker Solar Probe's orbit rapidly samples huge swathes of coronal structure leading to novel constraints on solar wind source regions
- Footpoint predictions for Parker are most accurate under quiet solar conditions with source locations concentrated in equatorial coronal holes
- We make an empirical determination of the Alfvèn surface and relate protrusions in it to underlying coronal magnetic topology

Correspondence to:
S. T. Badman,
samuel.badman@cfa.harvard.edu

Citation:
Badman, S. T., Riley, P., Jones, S. I., Kim, T. K., Allen, R. C., Arge, C. N., et al. (2023). Prediction and verification of parker solar probe solar wind sources at 13.3 $R_\odot$. *Journal of Geophysical Research: Space Physics*, *128*, e2023JA031359. https://doi.org/10.1029/2023JA031359

Received 31 JAN 2023
Accepted 20 MAR 2023

1. Introduction

Parker Solar Probe (Parker; Fox et al., 2016) is a NASA heliospheric mission launched in 2018 to explore closer to the Sun than ever before. Parker carries four instruments: The Electromagnetic Fields Investigation (FIELDS, Bale et al. (2016)), the Integrated Science Investigation of the Sun (IS⊙IS, McComas et al. (2016)), the Solar Wind Electrons, Alphas and Protons (SWEAP, Kasper et al. (2016)) and the Wide-Field Imager for Solar Probe Plus (WISPR; Vourlidas et al. (2016)). With the exception of WISPR, Parker carries only in situ instrumentation. Further, WISPR is designed to view scattered white light well off the limb. As such, although Parker captures

the local properties of the solar wind in situ in exquisite detail, remote observations of where the plasma came from at its origin on the Sun must necessarily be made by other instruments and spacecraft on Earth and in the heliosphere or by ground-based telescopes. Making such connections back to the Sun is integral to all three of Parker's primary science objectives (Fox et al., 2016).

1. Trace the flow of energy that heats and accelerates the solar corona and solar
2. Determine the structure and dynamics of the plasma and magnetic fields at the sources of the solar wind
3. Explore mechanisms that accelerate and transport energetic particles

Many remote observatories, both space-based (e.g., the Interface Region Imaging Spectrograph, De Pontieu et al. (2014)) and ground-based (e.g., the Daniel K. Inouye Solar Telescope, Rimmele et al. (2020)) have too small a field of view to observe the whole solar disk, or have high-resolution instrument modes with a smaller field of view (e.g., the Extreme Ultraviolet Imager (Rochus et al., 2020) on board Solar Orbiter (Müller et al., 2020)). As such, they require on-disk target coordinates as input to their nominal operations, and these coordinates must typically be provided hours to days in advance of the observation being made.

Therefore, to take full advantage of the array of solar observatories available, it is necessary to model the magnetic connectivity through the solar wind from Parker's location back to its origin low in the corona and derive target coordinates. Moreover, this modeling must be done as a *prediction*, meaning it is done without any feedback in the form of in situ data (Section 4.1) and using the most recent available boundary conditions which are assumed to be somewhat representative of the coronal conditions in the immediate future. Such predictions have been attempted by individual modelers since the mission launched (Kim et al., 2020; Riley et al., 2019; Stansby et al., 2019; Van der Holst et al., 2019; Wallace et al., 2022).

The statement of the basic procedure for source mapping is deceptively simple. At its core, we consider the plasma between the source and the spacecraft (including the corona and the inner heliosphere or solar wind) to be well described at large scale by ideal magnetohydrodynamics (MHD) and that therefore the magnetic field is frozen in to plasma parcels as they flow away from the Sun. Thus, the time history and origin at the Sun of a given plasma parcel measured in situ in the solar wind is simply estimated by magnetic field line tracing from the position of the measurement back toward the Sun (or identically, velocity streamline tracing in the solar-corotating frame, if the model includes the velocity field). See, for example, Stansby and Verscharen (2022) for the governing equations for field line tracing of a vector field on a numerical grid.

Despite the simple procedure, obtaining accurate results from this modeling task is far from trivial. Assessing its accuracy and uncertainty has been the goal of much recent work (e.g., Da Silva et al., 2022; Koukras et al., 2022; MacNeil et al., 2021). Our approach, which is the subject of Section 2.1, is to gather model estimates from a diverse array of models (Section 2.1.1), model parameters and physical boundary conditions, then form a distribution to assess the most probable source mapping and quantify the convergence. At several points in this work, the resulting mappings are illustrated using a potential field source surface (PFSS, Altschuler & Newkirk, 1969; Schatten et al., 1969) corona and a Parker spiral representation of the inner heliosphere (Neugebauer et al., 1998; Nolte & Roelof, 1973; Parker, 1958). See, for example, Badman et al., 2020; Koukras et al., 2022; Rouillard et al., 2020 and Section 2.1.1 for specific details of how the modeling works in this case.

There are numerous novelties to performing these predictions for the Parker mission due to its unique orbits, whose key features we illustrate in Figure 1. In the left panel we show the mission trajectory in inertial coordinates for which the very elliptical nature of the orbits is clearly illustrated. In the right-hand panel, the same orbits are shown in the solar-corotating (or "Carrington", Carrington (1863)) reference frame in which the Sun's angular rotation (25.38 day period) is removed, meaning only the spacecraft moves in these plots and solar wind stream structure can be plotted as static in time. This latter frame is, therefore, the most useful for understanding source mappings for Parker.

From these plots, we note that Parker's orbits evolve significantly throughout the mission. They are organized into families of progressively closer perihelia separated by Venus gravity assists. We refer to the portion of each orbit where Parker is close to the Sun and moves as faster or faster than solar rotation as an “encounter”, and abbreviate, for example, “Encounter 1” as E01.

In Figure 1, we contrast E01 (the very first perihelion of the mission from November 2018, which reached 35.7 $R_\odot$) and E10, the main subject of this manuscript which took place in November 2021 and was the first orbit

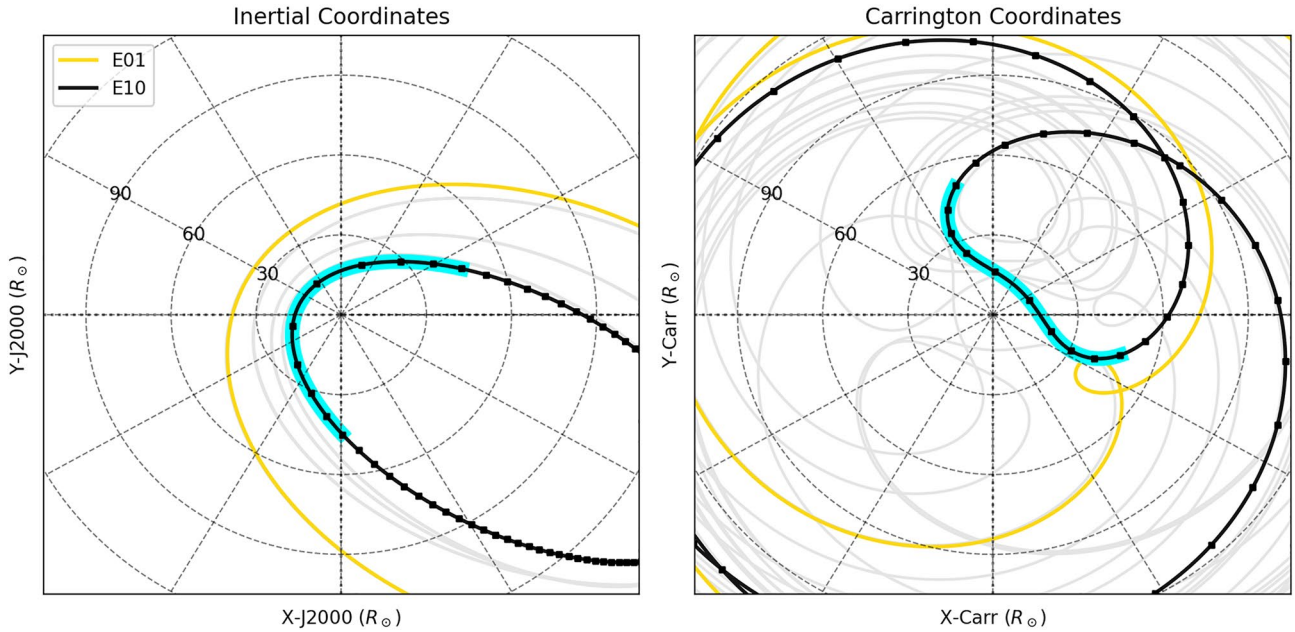

Figure 1. Orbital Geometry of the 13.3 $R_\odot$ orbit family. Parker's E10 orbital track projected into the solar equatorial plane is shown in black with E01 shown in yellow for contrast. Black squares are spaced 24 hr apart. Faint gray curves show the full prime mission trajectory (i.e., 24 orbits). The left-hand panel shows the inertial J2000 reference frame for which the orbit's elliptical nature and decreasing perihelion is clear. The right-hand panel shows the Carrington frame, which is most relevant for source mapping. This frame demonstrates the enormous range of solar longitude traversed by Parker in its latter orbits over just a few days around perihelion. Cyan shading shows the ~9-day interval of E10 where Parker co-rotates or super-rotates with respect to the Sun, which is the focus of this study.

to reach a perihelion of 13.3 $R_\odot$. The contrast shows that even relative to the record-breaking first perihelion, Parker's most recent orbits are dramatically closer to the Sun.

However, while the close approach distances are usually the headline of the mission, the angular motion in the co-rotating frame is equally as novel. The Carrington frame transformation reveals how Parker's perihelia include an interval where Parker moves faster than solar rotation and therefore moves prograde with respect to sources on the Sun. In the most recent orbits, this period has expanded to cover over 150° longitude, and the central 120° longitude is covered in less than 3 days (see the black squares in Figure 1, which are spaced 24 hr apart). This leads to an unprecedented set of measurements covering a huge spatial range in a very short period of time. As we will see in this paper, this leads to a powerful new way to verify source mapping and infer large scale coronal structure directly from in situ measurements.

The structure of this paper is as follows: In Section 2 we introduce the magnetic footpoint prediction campaigns carried out in support of each of Parker's perihelion passes. We summarize the methodology for collecting predictions and combining them to establish a consensus location. We then present in Section 3 an overview of the predictions made during Parker E10, the primary focus of this work. Next, in Section 4, we turn our attention to utilizing the Parker data after each perihelion to evaluate the predictions and highlight how Parker's spatial motion in its most recent orbit makes this evaluation stronger. We then contrast the E10 results predictions with early predictions for E04 and show under which coronal conditions our predictions are most accurate and convergent (Section 4.3). To close our analysis, we discuss how interpreting Parker measurements as large spatial cuts through coronal structure, we can use well-validated footpoint mapping to relate this structure to coronal magnetic topology and illustrate this with an example of a cut through the Alfvèn surface (Section 4.4). In Section 5, we discuss the key inferences and takeaways from the various analyses presented in the prior sections. Lastly, we close with Sections 6 and 7 where we present our major conclusions and identify directions for future work. Additionally, in Appendix A, we discuss miscellaneous practical aspects of making these predictions operationally and disseminating the results.

2. Parker Footpoint Prediction Campaigns

Since its fourth solar encounter (E04 January 2020), Parker has spent a significant portion of its perihelia passages on the Earth-facing hemisphere of the inner heliosphere. As a result, there has been a significant effort made to enable Earth-based observers to make coordinated observations of the specific locations on the Sun which source the plasma measured in situ by Parker (see Appendix A for a discussion of the practical aspects of these campaigns). These locations will be referred to as "(magnetic) footpoints" or "solar wind sources" interchangeably throughout this work. Although such remote-in situ connections have been attempted for as long as there have simultaneously been both types of solar observatories online (e.g., Nolte et al., 1976), achieving it with Parker has the potential to be much more robust and informative due to its close approach to the Sun and the subsequent reduction in processing of the solar wind plasma between emission and receipt. Such targeted observations are of vital importance for maximizing the science return of missions like Parker, resulting in a two-way benefit in which remote observations can be used to contextualize the in situ datasets, while the in situ data can then be traced back to remotely observed processes on the Sun to better understand the intrinsic physical processes. As mentioned earlier, achieving localized observational targets ahead of time is important to use many of the highest resolution instruments at Earth since their fields of view are much smaller than the solar disk.

2.1. Footpoint Predictions and Establishing a Consensus

A fundamental ingredient to achieving these coordinated observations is therefore making footpoint *predictions* in advance of each orbit. Making these predictions necessarily entails computational modeling since the in situ data that can later be used for verification (Section 4) has not yet been taken. For the Parker mission, this data is not even available near-real-time since the spacecraft attitude required to safeguard the system from solar radiation during perihelion precludes communication with Earth (Kinnison et al., 2020). The key challenge is how to produce the most accurate footpoints possible without in situ data constraints.

The modeling involves producing global numerical representations of the coronal and heliospheric plasma, flying Parker's upcoming trajectory through the model, and tracing inwards continuous magnetic field lines (or equivalently under the frozen-in theorem, velocity streamlines in the co-rotating frame if the model includes fluid flow) that connect Parker to a certain location on the Sun which is specified as a heliographic coordinate on the solar surface (i.e., longitude and latitude at the photosphere). In this work, we utilize predictions from several different models with differing internal physics and input boundary conditions, but all are broadly carrying out this same high-level task (see Section 2.1.1 for a discussion of some of the differences between the models run for E10).

We use this universality of the modeling task as our primary method for maximizing prediction accuracy and quantifying the uncertainty: We simply require each model to produce a prediction in the same format: CSV files with columns "Date", "Time", "Carrington Longitude" and "Carrington Latitude" and data entries extending from the time of the prediction through the rest of the upcoming encounter (see Badman et al. (2023) for examples). We then collect the data from these files and bin the heliographic locations into windows of time of arrival of the plasma at Parker (initially every 6 hr in the first iterations of this methodology, but more recently every hour as Parker's angular velocity at perihelion has increased). We treat the collection of locations in each window as an ensemble of predictions from which we want to establish a consensus source location and record some information about the spread in predictions to encode the uncertainty.

This consensus establishment process is illustrated in Figure 2. Following from panels (1)–(3), we show how a given ensemble is drawn from several different models (and within each model, variation in model parameters and input boundary condition, i.e., there is a sub-ensemble for each model). The overall ensemble is then fitted with a Kent distribution (Kent (1982), a.k.a. the 5-parameter Fisher-Bingham distribution or FB_5), which is the spherical analogue of an elliptical Gaussian in a 2D plane. This distribution behaves well on the whole sphere (i.e., it is not tripped up at the poles or by crossing periodic boundary conditions) and captures how concentrated the distribution is as well as the orientation on the sphere over which it is spread. The fit is performed with software implemented by Fraenkel (2014). Having fit the distribution, we then reduce the information down to the distribution peak, which we term the "source centroid", and a half-maximum contour (analogous to the full width at half-maximum of a 1D distribution) which is an ellipse encoding the uncertainty. The source centroid is interpreted as the "consensus" solar wind source that remote observers are advised to target (see section A2 for a discussion on the subtlety of the timestamp the target is valid for, a determination which has been actively evolving in recent iterations of this methodology).

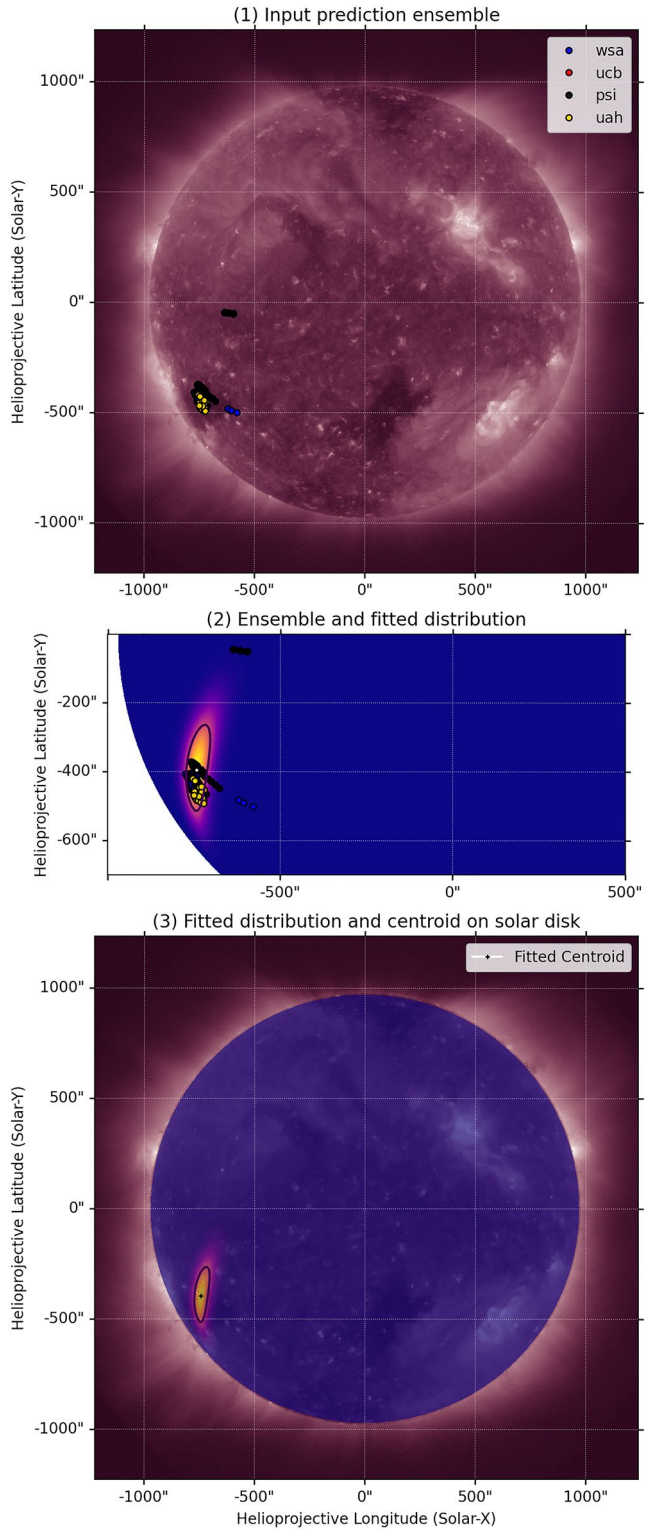

Figure 2. Steps for establishing consensus from an ensemble of footpoint predictions. (1) Footpoint predictions for a certain window of times of arrival at Parker supplied as Carrington longitude and latitude are gathered from different model predictions as an ensemble. (2) The ensemble is fitted to an elliptical Gaussian on a sphere with a Kent distribution (Fraenkel, 2014; Kent, 1982). (3) From the fit, the distribution centroid is the "consensus" source location, while the half-maximum contour of the distribution encodes the uncertainty.

2.1.1. Models Used for Footpoint Predictions for E10

The legend of Figure 2 indicates the four different model sources for which predictions were provided during encounter 10. We briefly outline the differences and specifics of each model uses to derive footpoint estimates.

- WSA results come from the Wang-Sheeley-Arge (WSA, C. N. Arge and Pizzo (2000); C. N. Arge et al. (2003); C. Arge et al. (2004)) model. WSA combines the potential field source surface (PFSS, Altschuler and Newkirk (1969); Schatten et al. (1969)) and Schatten current sheet (SCS, Schatten (1972)) models to specify the global inner and outer corona magnetic field, respectively, and an empirical relationship to prescribe the asymptotic solar wind speed on a grid on the outer boundary of the coronal model, which is typically set to between 5 and 21.5 Rs. Solar wind macro-particles are then propagated quasi-ballistically (i.e., ad hoc stream interactions are included to prevent fast streams from bypassing slow ones) outward from the model boundary to the satellite, carrying with them the memory of the photospheric footpoint of the magnetic field line on which they originated. For the Parker footpoint predictions, WSA models were run for ADAPT-GONG, ADAPT-HMI, and GONGz input magnetograms.
- UCB results come from PFSS modeling performed with pfsspy (Stansby et al., 2020) and ballistic mapping for the heliospheric part in a framework developed at UC Berkeley for supporting Parker's first orbit (Badman et al., 2020; Bale et al., 2019). In short, for a given magnetogram a PFSS model is run with some source surface radius R_{ss}. Parker's trajectory is then used to seed numerous Parker spiral field lines which are used to project Parker's position down to R_{ss}. At this point, field line tracing is performed using the built-in field line tracing tool in pfsspy to draw a field line from R_{ss} to $1R_{\odot}$. The longitude and latitude of this footpoint is then the prediction supplied. This process is iterated with different global magnetic maps (ADAPT-GONG and ADAPT-HMI, and ADAPT realizations therein (C. N. Arge et al., 2010; Arge et al., 2011; Hickmann et al., 2015)) and values of R_{ss} for a given prediction day.
- PSI predictions come from models run at Predictive Science Inc., which include (a) an independent PFSS solver (Caplan et al., 2021) and ballistic heliosphere, with steps similar to those of UCB, and (b) predictions from the Magnetohydrodynamics Algorithm outside a Sphere (MAS) (e.g., Riley et al. (2019); Riley et al. (2021)). For the MHD solutions, we map the solar wind ballistically back to 30 R_S, after which we trace along the appropriate field lines back to the solar surface. When the spacecraft is within 30 R_S, there is, of course, no ballistic component to the mapping procedure. As with UCB, the PSI team creates a suite of realizations using both ADAPT-GONG and ADAPT-HMI magnetograms (updated to 1200 and 0800 on the day of the prediction, respectively), together with a range of source surface heights for the PFSS model.
- UAH predictions come from the University of Alabama, Huntsville Multiscale Fluid-Kinetic Simulation Suite (MS-FLUKSS, Pogorelov et al. (2014); Pogorelov (2023); Singh et al. (2022)), which can solve the Reynolds-averaged ideal MHD equations for the mixture of thermal and nonthermal solar wind ions coupled with the kinetic Boltzmann equation describing the transport of neutral atoms. An adaptive mesh refinement technique can be employed for efficient high-resolution calculations. The MS-FLUKSS heliospheric MHD model is coupled with the WSA model (Kim et al., 2020), which uses both ADAPT-GONG and ADAPT-HMI input magnetograms, with the PFSS source surface height and the WSA outer boundary at $2.5_{\odot}$ and $10_{\odot}$, respectively. Hence, field line tracing is performed through the MHD domain down to 10 $R_{\odot}$ instantaneously at approximately 1 hr cadence, where the origin of the field line on the photosphere is already known, as described earlier for WSA.

3. E10 Footpoint Predictions

In the present work, we are primarily focused on the results of the prediction campaign for Encounter 10 (E10) which took place in November 2021, and was the first Parker orbit to reach a perihelion distance of 13.3 $R_{\odot}$, (the prior distance was 15.8 $R_{\odot}$ as of April 2021). As discussed in Section 1, in addition to the substantially closer perihelion distance, the newest orbits of Parker are also novel in their extremely large longitudinal coverage around the Sun in a very short time over perihelion.

E10 was a “partially on-disk” encounter where Parker's footpoints passed behind the west limb shortly after perihelion, and therefore had a small-scale prediction campaign (Section A1). Updates were issued on 2021/11/8, 2021/11/11, and 2021/11/15. Perihelion occurred on 2021/11/21 at 8 a.m. UTC, while limb passage was predicted to occur by 12 p.m. UTC the same day.

In Figure 3 we present the source predictions and derived consensus source locations produced at the time of E10, that is, prior to in situ data from that orbit becoming available for the last issued update for the

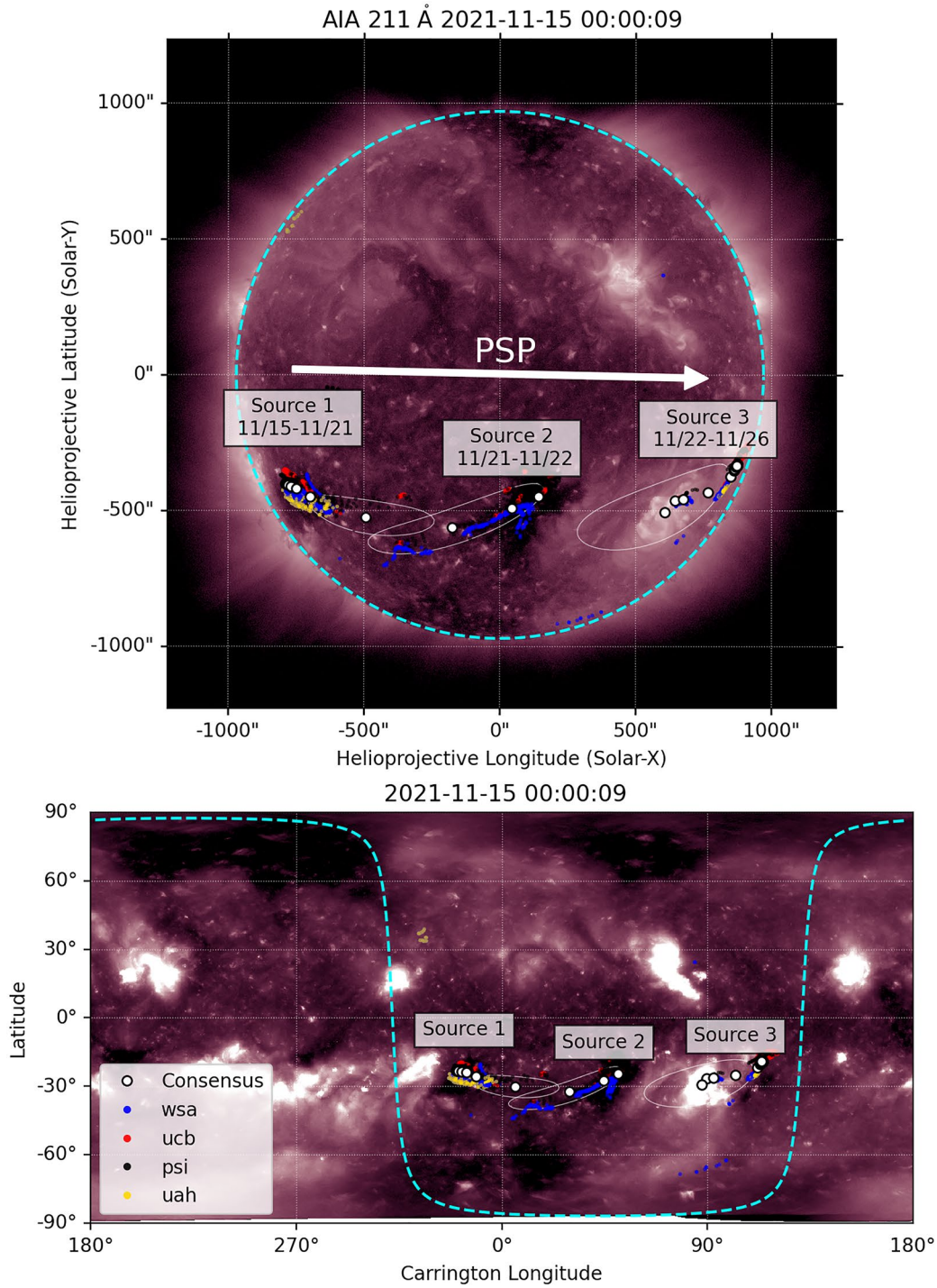

Figure 3. Summary of footpoint predictions for Parker Encounter 10. Both panels depict the encounter 10 predictions for Parker's footpoint connectivity as updated on 2021/11/15, superimposed on SDO/AIA 211 Å remote observations. The top panel is the helioprojective view from the date of the update, while the bottom panel shows a heliographic projective with EUV data from a Carrington rotation centered around the date of the update. Different colored dots show the distribution of predictions from different models (see main text), while the white points with black outlines show the consensus, and the faint white contours show the associated half-maximum contour (see Section 2.1). The footpoints track from left to right in time in both plots as Parker rotates faster than the Sun during perihelion.

encounter (2021/11/15). The two-panel figure shows the input ensembles as colored scatter points (refer to Section 2.1.1 for specifics on the ensemble members). The derived consensus and uncertainty ellipses are shown as white markers and white contours projected in both the helioprojective frame as seen from Earth on 2021/11/15 (top) and in the Carrington frame (bottom). The background texture is SDO/AIA 211 Å Extreme ultraviolet data (For the Carrington frame it is assembled from 1 solar rotation centered on 2021/11/15). A cyan dashed curve shows the same solar limb contour in both panels allowing the panels to be related to each other.

The top line of the prediction is straightforward to see from the figure. As annotated, the predicted footpoints (which move from left to right chronologically in both panels as Parker rotates faster than the solar surface) cluster in turn in a series of three isolated mid-latitude coronal holes in the southern hemisphere. All three are verifiable as dark regions in the EUV data. The first two have significant spatial extent, while the third is thin and extended. As will be verified later with magnetic modeling, all three are negative polarity and therefore the prediction also entailed suggesting Parker would not have any heliospheric current sheet crossings during this encounter.

Figure 3 also emphasizes the large range of solar longitude crossed by Parker during its latest encounters over a relatively short time. In fact, the entire traversal from one limb to the other shown in this plot takes place over just 9 days, with the bulk of that time occupied by Parker hovering over source 1 and source 3 as it respectively goes through inbound and outbound corotation with the Sun (see the date labels in the figure). We note that a subtlety not directly conveyed by the figure that although all three sources are visible on disk on the date the prediction was issued, the Sun continues to rotate as seen from Earth. As a result, source 3 rotates behind the limb before Parker reaches it. However, the first two sources were synchronously visible while Parker connected to them.

The predictions are also tightly clustered. For time intervals where Parker is predicted to connect to one of the three coronal holes, almost all ensemble members were located within the same coronal hole. There was no bifurcation. This led to high confidence in this prediction despite the lack of available in situ data at the time it was issued.

Note that of the consensus points (white circles) *not* located within the coronal holes, their location is driven by difficulties in the consensus fitting procedure when Parker is moving extremely rapidly across the disk. For this encounter, we still used six-hour windows for the consensus fitting. However, for this orbit, 6 hr near perihelion constitutes a large amount of longitudinal motion which causes some windows to contain ensemble members from two of the sources. When generating the consensus then, the fitted centroid was averaged between the sources, and the error ellipse grew large and protracted in longitude, as can be verified from the figure.

4. Prediction Evaluation

We now combine these predictions with in situ data obtained after the encounter. We discuss how we cast the data to spatial coordinates and then use it to evaluate the predictions, thereby inferring the global coronal structure.

4.1. In Situ Data and Ballistic Projection

We first introduce in situ data taken by Parker during encounter 10, specifically looking at the 9-day interval over which Parker was corotating or super-rotating with respect to the corona as highlighted earlier in Figure 1. In the left-hand column of Figure 4 we show (from top to bottom) timeseries of the radial component of the magnetic field (B_R) measured by Parker/FIELDS (Bale et al., 2016), the electron density (N_e) as measured by quasi-thermal noise (QTN) signatures (Moncuquet et al., 2020) from Parker/FIELDS/RFS spectrograms (Pulupa et al., 2017) and the solar wind radial velocity moment (V_R) from Parker/SWEAP/SPAN-i (Kasper et al., 2016; Livi et al., 2022). In the bottom panel, we compute the Alfvèn mach number $M_A = V_R/V_A$ where $V_A = B_R/\sqrt{\mu_0 m_p N_e}$ is the Alfvèn speed. The bottom panel is therefore a derived quantity from the three panels above. This derivation requires that the input data are all evaluated at the same timestamps. We therefore linearly interpolate all this data to a five-minute cadence, which is plotted in Figure 4.

Timeseries are the most common format in which in situ heliospheric datasets are typically presented, and for Parker they can still be used to extract immediate interesting properties of the encounter. For example, the radial magnetic field shows Parker remained in a negative polarity stream throughout the encounter, and its magnitude

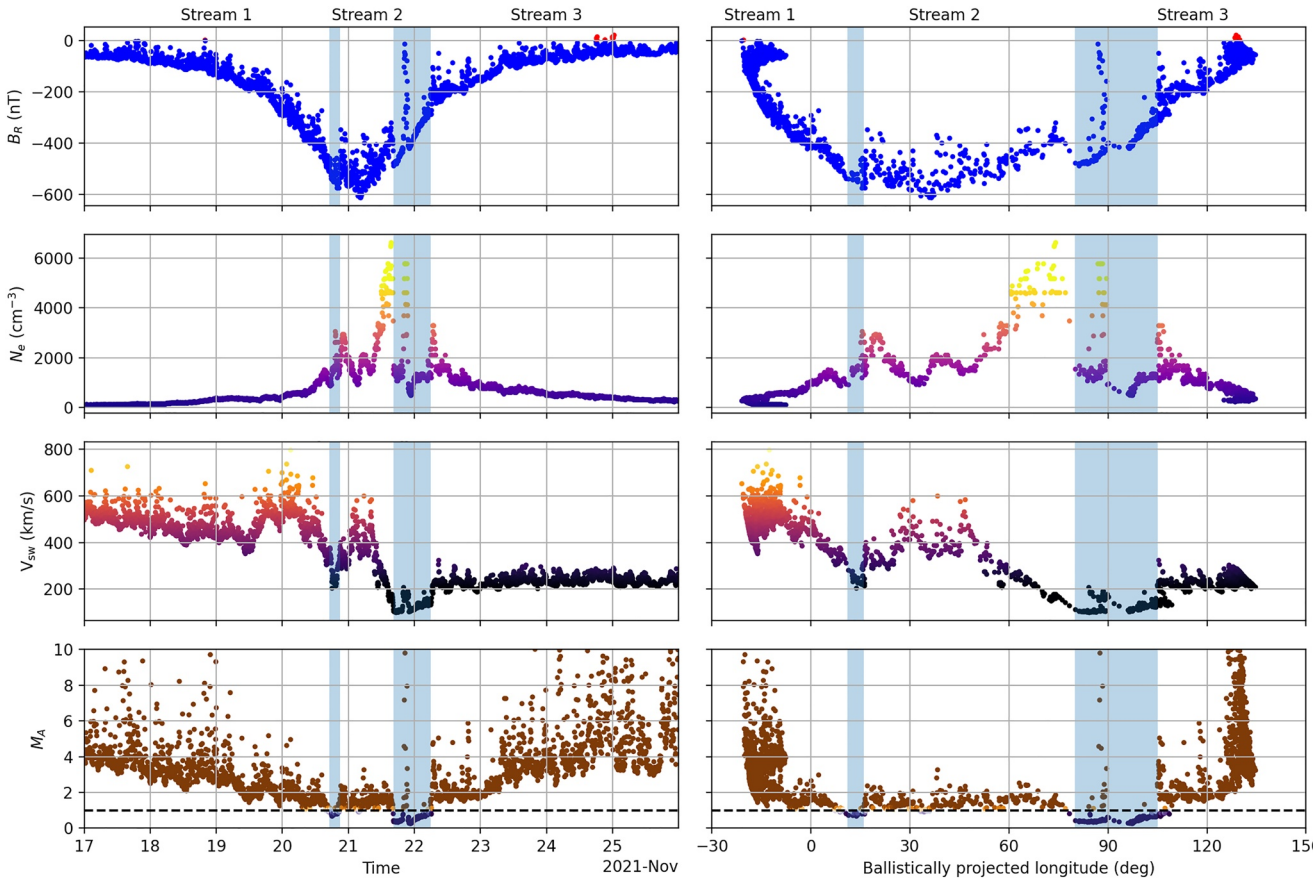

Figure 4. Temporal and spatial distribution of selected in situ data taken during Parker Encounter 10. From top to bottom, data shown are the radial component of the magnetic field vector (B_R, Parker/FIELDS), QTN-derived electron density (N_e, Parker/FIELDS/RFS), the radial component of the solar wind velocity (V_{SW}, Parker/SWEAP/SPAN-ion, proton channel moment), and the Alfvèn mach number ($M_A = V_{SW}/V_A$) where $V_A = B_R/\sqrt{\mu_0 m_p N_e}$ is the Alfvèn velocity). The left-hand panel shows the measured timeseries interpolated to a constant cadence of 5 min while the right-hand panel shows the same dataset but as a function of spacecraft position ballistically projected down to 2.5 $R_\odot$, as described in the main text. Colormaps for the bottom three rows highlight the relative variation of the relevant data set and allow features to be identified in both the left and right-hand columns. The colormap for the B_R profile (blue-red) simply encodes the magnetic polarity, which is essentially unipolar and negative.

scaled with the usual $1/R^2$ Parker spiral trend (Badman et al., 2021; Bale et al., 2019). The minimum in B_R represents the time of perihelion in the timeseries. The electron density is also seen to grow around perihelion. The velocity meanwhile shows that Parker measured moderately fast solar wind speeds in the inbound phase and then measured slow wind for much of the outbound period. The Alfvén mach number shows a smooth large-scale variation which is driven by the steady increase in the Alfvèn speed as the magnetic field strength increases. Near to perihelion, it is close enough to $M_A = 1$ that variation in stream structure drives excursions below the Alfvén surface. However, we remark that judging just from the timeseries, the significance of these periods may be underestimated as explained in the next paragraph. We will explore this Alfvèn surface structure further in Section 4.4.

However, to fully benefit from Parker's unique measurements, it is more powerful to cast the timeseries data returned by the spacecraft into spatial coordinates which co-rotate with the Sun. To achieve this, and subsequently to compare to coronal model footpoint predictions, we produce the Parker trajectory for a set of timestamps over the time period of interest (the same set used to interpolate the data for computing M_A). We then use the measured velocity at each interpolated timestamp to ballistically project (Badman et al., 2020; MacNeil et al., 2021; Nolte & Roelof, 1973) Parker's position at that time to a specific Carrington longitude (and latitude) at 2.5 $R_\odot$. Parker's unique orbit means this is not a linear or intuitive transformation. It causes the parts of the timeseries around corotation to collapse or fold back on themselves, while it stretches out periods near perihelion when Parker's angular motion is maximal, and thus reveals that structures or streams which might appear insignificant in the time series in fact have a substantial spatial extent.

Having applied the projection, we can now plot our interpolated datasets with the mapped longitude as the x-axis and observe how the measurements are distributed across the Sun. The results are shown in the right-hand column of Figure 4. As alluded to in the previous paragraph, the transformation strongly deforms the timeseries. We see that the small time period near perihelion, where field magnitude and Alfvèn mach number are relatively flat, constitutes most of the spatial motion during the encounter. The two sub-alfvènic intervals which appeared small in the time series are actually respectively 5 and 20° in longitudinal extent.

The most interesting transformation for the present work, however, is to the velocity profile. We see that it collapses into three distinct streams of similar longitudinal extent. The first two streams are relatively fast (400–500 km/s) while the last one is very slow (∼200 km/s). Traversing between each of the streams the solar wind speed drops and in both cases becomes sub-alfvènic for some or all of the transition. Recall that the general prediction for this encounter (without seeing the data) was for three sequential negative polarity coronal hole sources, the first two with significant areal extent while the third was narrow and extended.

4.2. Data-Model Comparison

In Figure 5 we illustrate the correspondence between the data introduced above and the footpoint predictions with the use of a representative PFSS model (meaning a model where the footpoints are near to the consensus points) to supply field lines and a model heliospheric current sheet (HCS). The HCS is located well above the latitudes covered by Parker in its orbit, which explains why the predictions are unipolar and negative polarity, and is consistent with the measured polarity as indicated by the colourization (blue) of Parker's trajectory in the figure.

However, E10 also yields a ready comparison between the solar wind velocity streams measured in situ and the predicted sources. This is illustrated in Figure 5 by the colored scatter points superimposed above the blue perihelion loop. These are annotated such that zero velocity would lie on the blue trajectory curve, and $V_R > 0$ causes a displacement upwards in latitude. This shows how the solar wind velocity spatial structure presented in Figure 4 directly corresponds to the source mapping between the three distinct coronal holes. To put it explicitly, the peaks in solar wind velocity in each stream occur when the source mapping is in the center of each coronal hole, while it slopes off toward the edges.

Figure 5 also illustrates how around the corotation intervals, the timeseries fold back on themselves. The upshot of this is that the initial fast wind data in Figure 4 from November 17-20 all correspond to the same coronal hole source: Its source first moves slowly eastwards over the center of the stream (but not reaching the east-most extent, since the velocity stays high), then reverses westwards. Beyond this point it continues on to the next two sources through the remainder of the encounter. A similar turnover is seen above source 3 for the outbound phase, but for continuously slow wind. Both intervals may therefore be regarded as “fast radial scans”, where the inbound is in fast wind, and the outbound is in slow coronal hole wind. Such scans are very interesting targets for studies that aim to study the same stream at multiple heliocentric distances (e.g., Davis et al. (2023)).

4.3. Encounter 04 Comparison - Coronal Conditions for Accurate Source Predictions

In the previous section, we showed multiple independent lines of evidence that our prediction campaign for Encounter 10 was highly successful. In this section, we briefly contrast this encounter with another to comment on the coronal conditions under which footpoint predictions are most accurate.

It is evident that time-dependent phenomenon will disrupt the accuracy of our footpoint estimates, since the models we run (see Section 2.1.1) are all time-independent. Further, they explicitly assume that the current state of the corona will remain the true state for some days into the future, since this is necessary to run predictions. Such time-dependence is ubiquitous in times of high solar activity. As such, we might assume that the condition for accurate predictions should be intervals of low solar activity. However, here we show that “low solar activity” is not a sufficient condition for accurate estimates.

In Figure 6 we present prediction ensembles (not consensus, but all modeler contributions) for Encounter 04 (January 2020, top panel) and Encounter 10 (November 2021, bottom panel) in the Carrington frame. We display the Parker perihelion trajectory for both encounters and color by the measured polarity (blue: $B_R < 0$, red: $B_R > 0$). We also choose a representative magnetogram date for both encounters and derive (via PFSS modeling) a HCS curve using both GONG and HMI-derived ADAPT global magnetic maps (respectively, black and gray curves in

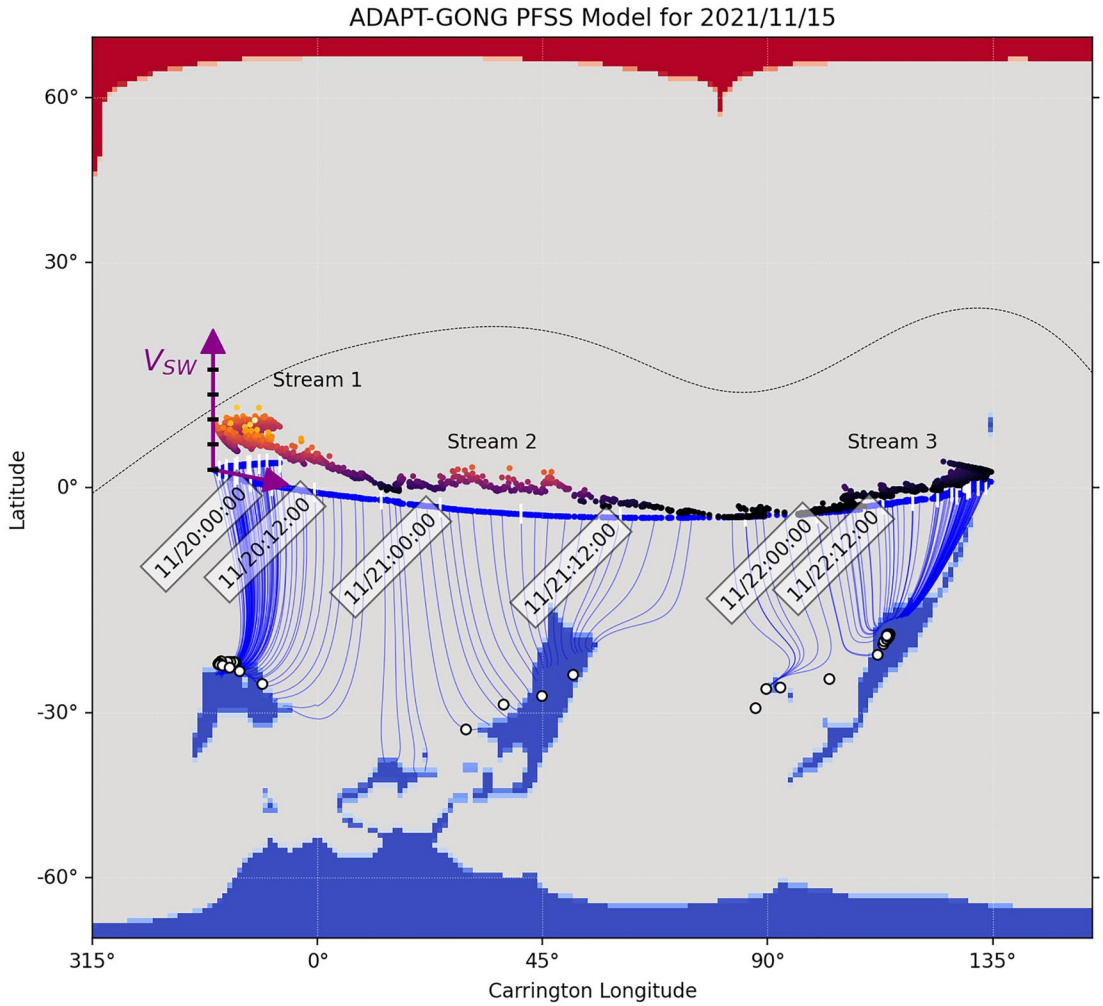

Figure 5. Correspondence between in situ stream structure and magnetic field mapping. A representative PFSS model (ADAPT-GONG 2021/11/15, 2.5 Rs source surface height) is used to generate field lines connecting the ballistically mapped Parker trajectory (blue, indicating consistent measured negative polarity by Parker/FIELDS) to its sources. Blue/red shading indicates the locations of coronal holes in this model. A narrow dotted line indicates the neutral line/heliospheric current sheet from the model. White markers indicate the consensus footpoint locations shown in Figure 3. The dark/light colored trace depicts the Parker/SWEAP/SPAN-i data shown in Figure 4 as a function of source surface longitude, allowing the thermal plasma stream structure to be visually associated with the source mapping. It's variation is plotted relative to the latitude of Parker's trajectory. White vertical bars indicate six-hr separation in the trajectory as Parker moves from left to right.

the plots) and a coronal hole map from the ADAPT-GONG magnetogram (modeled open field locations). In E04, we also keep track of GONG and HMI-based predictions by differentiating the markers as circles and diamonds, respectively.

We observe that during Encounter 04, the predictions were extremely bifurcated: All models (different colors) were predicting portions of their ensembles to be in the northern or southern polar coronal holes at similar longitudes. Not only was this instantaneously true for the prediction depicted in Figure 6, but additionally the ensemble members from the same magnetogram type could switch hemisphere from one prediction update to the next as the most recent magnetograms were updated. Typically during this campaign, footpoints derived from GONG-based magnetograms clustered in one hemisphere and HMI-based magnetograms clustered in the other. This is most obviously seen in Figure 6 around 0 longitude where diamonds (HMI) are all in the northern hemisphere, and circles (GONG) are in the southern hemisphere. Although harder to see, this also occurs in the perihelion loop (around 90°) where the footpoints are denser.

The root issue here was that the coronal conditions for this encounter were extremely quiet and solar minimum-like: The open magnetic field was all confined to the polar coronal holes and the resulting HCS curve was very flat and

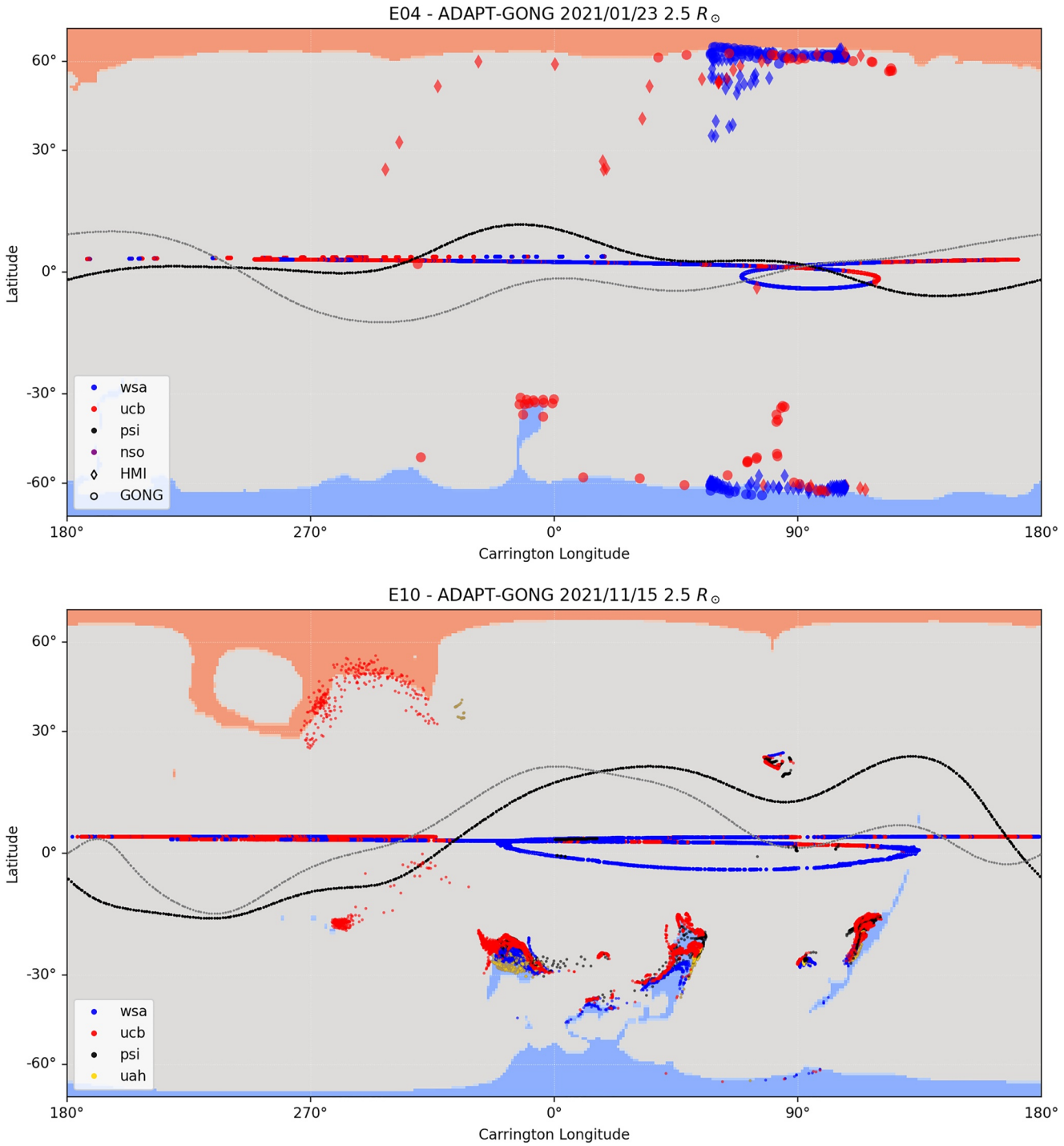

Figure 6. Footpoint prediction distribution for different coronal configurations. Top panel: The footpoint predictions made for Parker Encounter 04 (January 2020) from different models and input magnetograms. The extremely flat HCS in the vicinity of Parker's perihelion leads to strongly bifurcated and unstable predictions split between both polar coronal holes, and bifurcation between models driven by ADAPT-GONG (circles) versus ADAPT-HMI (diamonds)-based magnetograms. Bottom panel: E10 footpoint predictions (see Figure 3). A fainter gray HCS contour in both panels show how the ADAPT-HMI neutral line for the same magnetogram date differs from the equivalent ADAPT-GONG one.

almost perfectly equatorial. Due to Parker also orbiting very near the heliographic equator, this meant that only a small shift in the model HCS line would move Parker's location from one side of the streamer belt to another. These shifts were small enough to be caused by the normal variation of changing the on-disk portion of the magnetogram by 1 day and, as illustrated by the black versus gray HCS, by varying which instrument is used to assemble the magnetogram even if issued on the same day.

Additionally, even assuming predictions did converge on one hemisphere or another, when the only source is the edge of the featureless polar coronal hole, it is hard to be accurate since predictions essentially follow the longitude of the ballistically propagated field line. Thus there is a large spread in longitudes for a given prediction window which is constrained not by the well-modeled coronal hole topology, but rather by the crudely modeled heliospheric field lines.

The contrasting situation for E10 can be seen from the bottom panel of Figure 6. As we have reported in prior sections, the magnetic footpoints from all different modeling sources and input boundary conditions clustered very tightly on single well-defined sources. This occurs because the heliospheric current sheet is tilted up and away from the orbit of Parker significantly enough that small perturbations in the model from differing magnetograms (again, visually compare the black and gray curve) do not cause any magnetic separatrices to cross Parker's trajectory at perihelion. Further, because each source was an isolated mid-latitude coronal hole, each expands in the model to cover a large region in the outer corona, so that a large portion of Parker's orbital path maps down to a much smaller region. This means that instead of the spread in footpoints being typically set by the spread in ballistically-mapped longitudes, it is instead set by the size of the coronal hole itself, which is much smaller (Koukras et al., 2022).

Finally, these contrasting campaigns also show how the much larger corotation loop in the most recent orbits also helps the situation by causing the connectivity to move between very different sources in the same perihelion. Thus the signatures of source changes, as shown in previous sections, are much more obvious in the in situ data.

Thus we conclude that the most robust situation for source mapping (for a near-ecliptic spacecraft) is not the most quiet, solar minimum-like conditions, since a flat featureless corona gives rise to difficulties navigating the HCS separatrix when trying to predict footpoints. Instead, we do indeed benefit from low solar activity in that it negates the impact of time-dependent phenomena, but we also require that there be strong perturbations to the heliospheric current sheet, and correspondingly, mid or equatorial coronal hole sources which cause such perturbations. Both the presence of the warped current sheet and isolated coronal holes contribute to reduced uncertainty in our footpoint predictions.

4.4. Inferring Global Coronal Structure: The Alfvèn Surface of E10

In this last analysis section, we demonstrate how combining the in situ measurements with the verified field line mapping allows powerful inferences of global coronal structure.

In the bottom panel of Figure 7 we display Parker's Carrington-frame trajectory for E10 projected into the heliographic equatorial plane and colourize it by the Alfvèn mach number following the same color normalization as in Figure 4, which clearly shows the spatial extent and locations of the two sub-alfvènic intervals.

On top of this, we superimpose a simple construction to create a visual representation of the topology of the Alfvèn surface. Following (Liu et al., 2021, 2023), we take Parker's heliocentric distance as a timeseries and divide it by M_A where we smooth the data via a rolling 20 min (4×5 min data points) window. Recombining this modified radius coordinate with Parker's Carrington longitude gives us the black curve which necessarily intersects Parker's orbit when $M_A = 1$, is further out than Parker when $M_A < 1$ and closer in that Parker when $M_A > 1$. The curve is not intended to be quantitative in how much further out or in it is relative to Parker when $M_A \neq 1$, but does qualitatively capture the large-scale undulations in the surface which are implied by the data. However, we note that this construction as used by Liu et al. (2021); Liu et al. (2023) is the limiting case of physical scaling assuming the radial magnetic field and plasma density vary as $1/r^2$ and a constant solar wind speed (e.g., Weber et al., 1967). In particular, the latter assumption of constant wind speed needs quantitative re-examination with Parker now measuring substantial solar wind acceleration (Dakeyo et al., 2022; Halekas et al., 2022), but for the purposes of the present manuscript is sufficient to describe when Parker is above or below the Alfvèn surface.

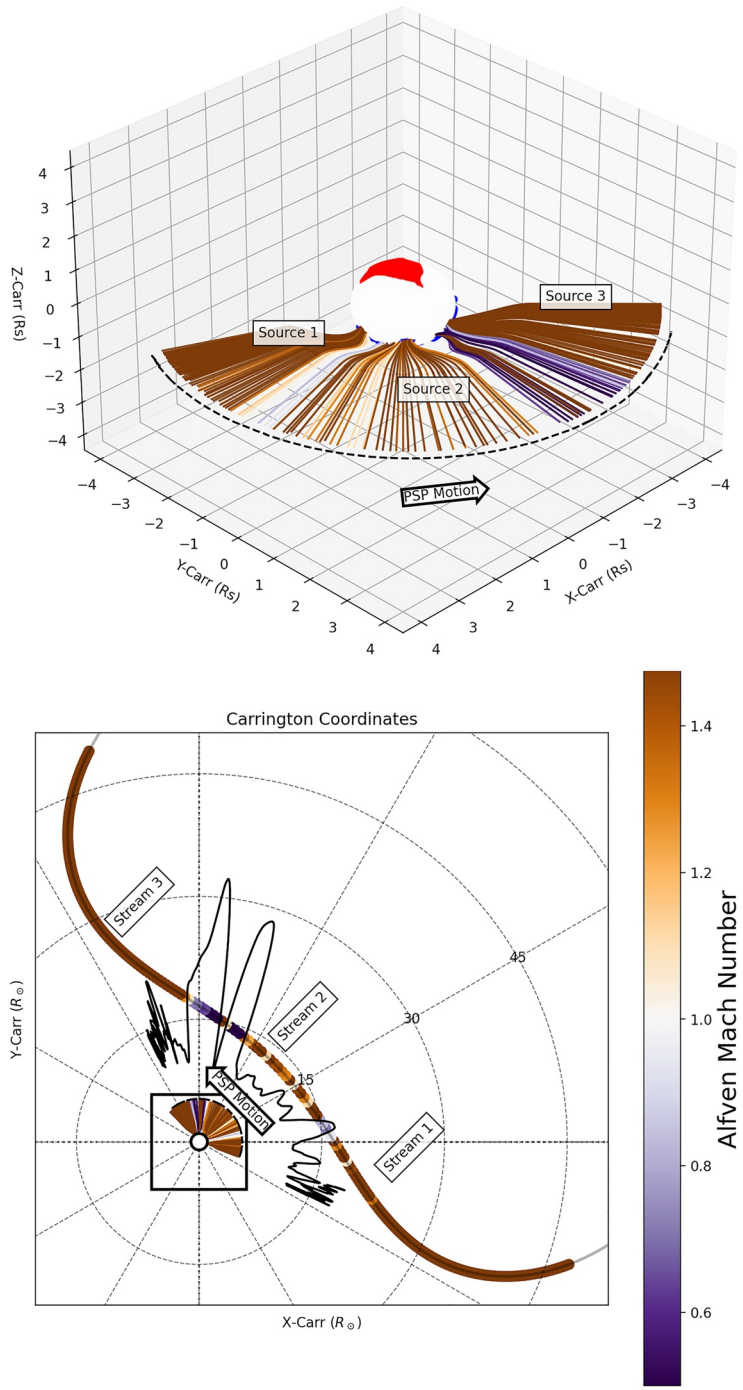

Figure 7. Empirical constraints on the shape of the Alfvèn surface and source region relations. The bottom panel shows Parker's E10 trajectory (bottom right to top left in time), colourized by measured Alfvèn Mach number. An empirical estimate of the Alfvèn surface constrained by the measured $M_A = 1$ crossings is shown in black (see main text). A small square shows the region depicted in the top panel which shows PFSS field line mappings from 4 $R_\odot$ down, colourized by the measured Alfvèn mach number so they can be related to the Alfvèn surface structure above. Both instances of sub-alfvènic wind (corresponding to an outward protrusion in the Alfvèn surface) are associated with pseudostreamer magnetic topology as in Kasper et al. (2021), although the first instance also appears to coincide with a traversal of a CME leg (McComas et al., 2023).

Thus we see the Parker data combined with its unique orbit allow estimation of large-scale properties of the corona and imply that the Alfvèn surface is typically within 13 R_S but has protrusions outwards which Parker has crossed. This empirical finding is interesting in its own right and consistent with a "wrinkled surface" as in Liu et al. (2023), as well as the lower ranges of prior estimates of the Alfvèn surface altitude, for example, (DeForest et al., 2014; Wexler et al., 2021). However, given the excellent validation of our source mapping for this time interval, we can go one step further and relate this empirical structure to the coronal magnetic topology.

In the top panel of Figure 7, we present the same field line mapping for E10 as was depicted in Figure 5 from a 3D isometric view, and this time use the color of the Alfvèn mach number mapped from the relevant timestamp in the Parker measurements. This shows us that the sub-alfvènic regions (where the colorscale goes from white to dark blue) occur over the unipolar magnetic separatrices between the individual coronal hole sources (pseudostreamers).

5. Discussion

In this work, we presented the full cycle of efforts made to predict Parker's solar wind sources for the purpose of facilitating coordinated observations, and subsequent evaluation methods to check the accuracy. We exemplified this with the specific campaign for Parker encounter 10, which was the first orbit to reach a perihelion distance of 13.3 $R_\odot$. We showed that these most recent orbits provide new tools for the prediction evaluation, using the huge and rapid sampling of spatial structure, and showed that E10 was particularly accurate. We used this example in contrast to a less accurate encounter (E04) to comment on the coronal conditions when such predictions are most accurate. Lastly, we showed how the spatial structure implied by these recent direct measurements can be connected with the magnetic topology of the corona and made novel inferences about the shape of the solar alfvèn surface as it relates to the presence of pseudostreamer topology (and resulting slow solar wind) low in the corona.

In Section 2, we presented a detailed account of the methodology used to make footpoint predictions for each encounter of the Parker mission. Our approach is model agnostic in the sense that it regards predictions from all different models as ensemble members from which a probability distribution is fitted, and then a consensus source location is extracted as the location of maximum likelihood.

In Section 2.1.1, we discussed the footpoint modeling procedure and the specific models used in this work. It is worth remarking briefly on the shared limitations of these models. Although the MHD models used are much more sophisticated than the PFSS models in terms of constituent physics, they are all time-independent and driven by the same set of boundary conditions. A key assumption for the source estimates is that our model of the corona and heliosphere remains valid for at least the time it takes a solar wind plasma parcel to propagate out to Parker. While this is undoubtedly a better assumption for Parker than, for example, 1 au connectivity, it does necessarily mean there is unmodeled physics not present in our ensemble. Another missing element is that our models are all smooth and relatively low resolution, meaning they do not contain any waves or turbulence. These effects could lead to plasma parcel random-walks and therefore field line meandering (e.g., Chhiber et al. (2021)).

However, as we saw in Section 4, regardless of this missing physics, our footpoint predictions under the right conditions (Section 4.3), and especially for Parker E10, do correspond well to in situ data at large scales. It is nevertheless worth being cognizant of these subtleties and realizing that large scale accuracy does not automatically mean accuracy at arbitrary precision (e.g., at scales much smaller than the source coronal holes).

In Section 3 we showed an exposition of the prediction results for E10. Over 9 days between inbound and outbound corotation, Parker was predicted to connect to a series of three negative polarity equatorial coronal holes, with the traversal between all three taking place in ∼2 days around perihelion (21 November 2021). Prior to having any in situ data to validate, there were already at least two reasons to be confident in the prediction. First, the ensemble of footpoints obtained from different models and boundary condition choices was tightly clustered and consistent. Second, the sources the predictions clustered on were verifiable in synchronous EUV images available at the time of the prediction.

Then, in Section 4, we explored the process of evaluating the predictions both for E10 and more generally. In Section 4.1 we presented in situ timeseries data from E10 and showed how the motion of Parker distorts the data profiles when it is cast into spatial coordinates. In Section 4.2, we examined how the spatial coronal structure

implied by the thermal plasma measurements made by Parker for E10 provided a very clear validation of the prediction in addition to predicting a consistent (negative) magnetic polarity.

In prior encounters, magnetic polarity has been our main discriminator in evaluating the predictions. Although the constraint can be somewhat stronger if there is an HCS crossing inside the encounter (where polarity in the data clearly changes from one sign to another, e.g., Badman et al. (2022)), in general, this is a rather weak source verification method since it can only verify that the predicted source was located in the correct magnetic sector but cannot discriminate between particular coronal holes or other sources.

However, the velocity stream structure correspondence is a much more powerful constraint as it directly addresses the structure and morphology of the sources. The first two streams had moderately fast wind at their peaks, while the third was continuously very slow. The first two coronal holes accordingly were relatively large and shaped such that they clearly had an exterior boundary and a central region where the field undergoes less non-radial expansion. The third, meanwhile, was thin and extended, suggesting almost all open flux emanating from it necessarily has a high expansion factor. The relationships between these coronal holes and the peak solar wind speeds conform well with the expectations of empirical relations between expansion factors and solar wind speed (Wang & Sheeley, 1990; C. N. Arge & Pizzo, 2000) as well as the distance from the coronal hole boundary (Riley et al., 2001; C. N. Arge et al., 2003). Further, the minima in velocity between the streams align well with unipolar separatrices, both while traversing pseudostreamers (around 15° and 100°) and in approaching (but not crossing) the HCS around 60°, which is consistent with prior associations between such separatrices and slow solar wind (e.g., Antiochos et al., 2011; Wang et al., 2012), especially slow solar wind dominated by alfvènic fluctuations (e.g., Panasenco et al., 2020) which is nearly ubiquitous in Parker observations (Bale et al., 2019).

This comparison method as a whole is a major novelty of Parker's most recent orbits that relies on the fact that Parker crosses a huge range of longitudinal distance around the Sun in a very short time. Earlier in the mission, Parker's perihelion hovered for 2 weeks over a very small region of the Sun (Badman et al., 2020; Bale et al., 2019). Other missions have only ever moved across the Sun's surface in slow retrograde motion (similar to the Earth) and at much larger heliocentric distances meaning temporal evolution of the corona and stream interaction and evolution are much harder to disentangle from the original coronal source structure.

In Section 4.3, we investigated under which conditions our footpoint predictions were accurate with reference to E10 (for which we had excellent validation of the predictions), and E04 (for which the predictions were extremely uncertain). The two situations were interesting to contrast in that E04 occurred during extremely quiet solar minimum conditions, while E10 occurred later in the solar cycle. The key difference was that since there is intrinsic noise in the position of the heliospheric current sheet when considering model results from different magnetograms and model codes, a flat, near-equatorial current sheet means the footpoints of a near-equatorial spacecraft such as Parker are quite unstable: small amounts of variation can cause the HCS sepatatrix to cross the spacecraft trajectory unpredictably, and change the footpoint location drastically. By contrast, in E10 the HCS was substantially warped and located well away from where Parker spent the encounter. This meant that small amounts of model-model variation barely changed the footpoints since the source coronal holes appeared near-universally in all prediction ensemble members. Additionally, while there was solar activity on the Sun during E10, Parker's orbit was fortuitously aligned with quiet regions without significant active region or transient activity.

Finally, in Section 4.4, we explored how the combination of in situ data from Parker's unique orbit, and source mapping for E10 gave us insight into the global structure of Alfvén surface. Specifically, we associated the two sub-alfvénic intervals of the encounter with unipolar separatrices (pseudostreamers) between neighboring solar wind streams, similar to the first such sub-alfvènic interval explored in Kasper et al. (2021). It is not a surprising association since pseudostreamers are generally thought to be a contributing source of the slow solar wind (Wang et al., 2012; Wang & Ko, 2019; Wang & Panasenco, 2019) and do not have a current sheet so maintain a strong B field throughout the structure. It is also a similar association to that highlighted recently by (Liu et al., 2023) who associate earlier sub-alfvènic crossings of Parker with overexpanded field from the edge of coronal holes, a structure they term a “low Mach-number boundary layer” (LMBL). We also comment that the radial scans on the inbound and outbound portions of the orbit allow the same portion of the surface to be estimated over an extended period of time. Our scaling to reconstruct R_A resulted in a surface which was roughly constant, however, there was still a finite thickness due to noise in the input data. This will be interesting to compare in future work with turbulent expectations of the thickness of the Alfvèn surface (Chhiber et al., 2022) and allowing the solar wind to accelerate self-consistently (e.g., Dakeyo et al., 2022).

The two individual sub-alfvènic intervals bear some discussion. The first one which occurs between the two fast wind streams is relatively narrow (about 5° longitude) and the mach number only reaches ∼0.9, implying it is a marginal crossing. Additionally, it occurs at the same time as Parker is thought to have crossed through the leg of a slow-moving CME released earlier (McComas et al., 2023), thus it is likely the Alfvèn surface location is perturbed by this transient disturbance. Since CMEs are typically faster than the ambient solar wind they plow through, it is possible the Mach number would drop further if Parker traversed the separatrix earlier.

The second interval is a more substantial sub-alfvènic crossing spanning over 20° of longitude and with M_A reaching as low as 0.1. Additionally, embedded in the stream is a sharp excursion back into the super-alfvènic regime driven by a sudden drop out in the magnetic field. The longitude where this occurs (and the turbulent properties therein, Zhao et al. (2022)) is consistent with Parker having a local close approach to the HCS, depending on the model chosen from the prediction ensemble (see e.g., the difference between the gray and black HCS in the bottom panel of Figure 6). Therefore Parker may be sampling a relatively non-trivial region of plasma in which pseudostreamers and the solar helmet streamer interact with each other and create a complex undulation in the Alfvèn surface.

With this Alfvn surface investigation, we are showing that magnetic topology low in the corona has a directly traceable imprint on the near-Sun solar wind - namely the outward protrusions in the Alfvèn surface, over a large range of solar longitude as probed by the unique orbit of Parker. This traceability between sources to make powerful inferences about the corona and heliosphere has also recently been explored by (Bale et al., 2023). Those authors use the clearly defined first two coronal holes studied here to examine the acceleration mechanism of the fast solar wind, and were able to convincingly tie the predicted solar wind signatures of interchange reconnection of mixed polarity field within the open field regions to in situ signatures present in those two solar wind streams.

6. Conclusions

Here we summarize our overall findings from this study.

We demonstrated our methodology for predicting the magnetic footpoints of Parker ahead of its perihelia passes, including our method to improve accuracy and quantify uncertainty via establishing a consensus footpoint from ensembles of predictions from different models and boundary conditions. We illustrated via studying Parker Encounter 10, that such an approach can and does work, since when the footpoints are most accurate, the predictions across different modeling approaches converge to the same sources.

The orbital dynamics of Parker's most recent perihelia enable the interpretation of the in situ timeseries data as a spatial prograde cut through a substantial portion of the inner heliosphere and outer corona in a very short time (over 120° in 3 days). This rapid spatial cut will only grow in scale as the mission perihelion further shrinks.

This spatially-interpreted data enables a novel and powerful way to evaluate source mapping predictions for Parker: The thermal plasma components measured by Parker/SWEAP (Kasper et al., 2016) exhibit clear longitudinal stream structure. This structure can be directly traced to the transitions between different sources. Enabling this is.

1. The large spatial scale of the perihelia, meaning significantly distinct sources are sampled sequentially.
2. The rapid motion, meaning that the coronal structure does not have time to evolve substantially between sources, and therefore is appropriately modeled by a single time-independent model.
3. The extremely close distance of Parker to the Sun, meaning that the solar wind is much less processed and the streamlines are all near radial so stream interactions do not disrupt the stream structure to a significant extent.
4. The relatively favorable alignment of the orbit with the Earth, allowing the most relevant regions of the photosphere to be observed near synchronously with the magnetograms which are the fundamental boundary condition of the individual models.

For E10 specifically, this correspondence was especially clear and took the form of three clear solar wind velocity streams corresponding to three distinct coronal hole sources of the same (negative) polarity. Pseudostreamer separatrices between the different unipolar sources corresponded to local minima in solar wind speed and additionally locations where Parker's crossed the Alfvèn surface. The different sizes and shapes of the coronal holes correlated well with the wind speeds (fast wind for the first two and slow wind for the third).

Next, using E10 as a case study of "successful footpoint predictions", the conditions under which such predictions are accurate were illustrated by contrasting with Encounter 04 (January 2020), when the prediction quality was much lower, even though there was almost perfect solar minimum conditions. In both cases, there was very low solar activity at the longitudes that Parker explored during in encounter, however, this was not a sufficient condition for accurate footpoints. An additional ingredient was the presence of a significant inclination or warping in the HCS, such that small day-to-day or magnetogram-to-magnetogram model variation does not significantly move magnetic separatrices with respect to Parker's trajectory.

For the E04 results where the footpoints were strongly bifurcated, it was observed that footpoints were more similar among model results driven by the same magnetogram than by different models driven by the same magnetogram, implying the input boundary condition is at least as important as the physics of the model for the application of field line tracing (see also Riley et al. (2006); Badman et al. (2022)).

Lastly, moving beyond their role in source validation, the in situ spatial cuts themselves constitute large-scale slices through the global structure of the outer corona and inner heliosphere. Combined with the footpoint mapping, we can associate such structure with underlying magnetic topology. We demonstrated this with the measurements of the Alfvén Mach number for E10 and found that it implies an average surface just below the current closest approach (13.3 $R_\odot$), but also a wrinkled surface with narrow protrusions which cross Parker's trajectory (see also Verscharen et al., 2021; Liu et al., 2023). By associating these protrusions with the well-validated source mapping, we observed they appear to occur over slow solar wind streams emanating from the tips of pseudostreamers or at least the overexpanded edges of coronal holes, as was reported for the first such crossing (Kasper et al., 2021).

7. Future Work

Parkar's prime mission includes at least 10 further orbits (at the time of writing), the latter eight of which will all be even closer and therefore consist of an even larger spatial cut through coronal structure. Therefore we anticipate repeating the footpoint prediction and validation exercise presented here for all such orbits. There will be further iterations to make these as accurate, useful and practical as possible.

For example, as shown by the pipeline in the associated GitHub repository for this work (Badman et al., 2023), the analysis required to produce the predictions is very close to being automated. Therefore we aim to complete this process and make available the pipeline as a python script. Some human interaction is still needed to produce text descriptions of the predictions to account for such factors as solar activity or multiple source centroids (Appendix A).

Additionally, an as yet untapped direction for improving the accuracy of our footpoint predictions is to use complementary near real-time observations from 1 au spacecraft and Solar Orbiter (SolO; Müller et al., 2020) where available to narrow down the parameter space of the models used in the footpoint ensembles. Specifically, magnetic polarity measurements of the most recent orbits to cross the Carrington longitudes of Parker's upcoming orbits can be used to constrain the position of the heliospheric current sheet and reject any model results which are clearly inconsistent with this. As another example, for cases (such as E10) where the predicted sources are coronal holes with specific morphology, the most recent direct EUV observations can be used to confirm or refute their existence, or to choose ensemble members where the open field morphology is most similar to the EUV observations and weight them higher.

A further key issue for producing useful coordinated observations which was not deeply addressed in the present work is the issue of transit timing from Sun to Parker. One objective of such observations is to directly observe the injection of impulsive signatures on open field lines at the coronal base and associate them directly with in situ signatures at Parker. The time lag between such emission and receipt depends on the disturbance (whether it is advected with the solar wind, or propagates at an MHD wave speed in the solar wind), but can be of order hours to tens of hours. At peak angular velocity, Parker can move from one source to another *at this same timescale*. Thus, when providing a footpoint and associated timestamp, estimating the transit time can be important. Since E10, this consideration has informed an additional component in the prediction files of an "emission time" and "receipt time" with an unsophisticated ballistic estimate. For further encounters, especially those closer to the Sun, this issue will become even more pronounced, so the estimate should be improved using, for example, the most recent available SolO data, to constrain a Parker solar wind curve and integrate to provide an accurate transit time.

As mentioned in Section 5, time-dependence of the models themselves is also currently not accounted for other than in the updating of the magnetic map boundary conditions as often as possible. Time-dependent phenomena such as waves and turbulence or just the development of stream interactions is an obvious direction to improve the modeling input itself to these procedures. Especially valuable would be using codes that directly follow test particles or plasma parcels through the model, rather than relying on smooth magnetic fields. While such modeling is vastly more computationally expensive than the tracing reported in this work, even one or two examples which can be compared to the results of time-static field line tracing would allow better estimates of its accuracy and precision in the absence of time-dependent effects.

Lastly, there are numerous interesting directions to pursue with regard to empirically constraining the alfvèn surface, a key boundary mediating between coronal and solar wind physics (e.g., Weber et al., 1967). Specifically, the scaling we used ($R_A = R_{PSP}/M_A$) following Liu et al. (2021); Liu et al. (2023) should be revisited and performed more carefully with the most recently available information about how the solar wind quantities scale with radius, for example, (Dakeyo et al., 2022; Halekas et al., 2022). This scaling yielded outward protrusions which are likely unphysically high, since they imply Parker would have measured sub-alfvènic excursions as early at its first perihelion, which it did not. There are now several orbits for which curves such as that depicted in Figure 7 can be derived for and the source regions compared. Further, intervals such as the radial scans, or conjunctions with spacecraft can be used to investigate how stable R_A is in time and how universal the radial scaling is. Lastly, as predicted here and in Liu et al. (2021); Liu et al. (2023), the latter orbits of the Parker mission are likely to reach the average R_A value implied by our scalings, it may imminently be possible to contrast differences crossings of protrusions over special solar wind streams with samples from inside the "normal sub-alfvènic"' corona.

Appendix A: Practical Aspects of the Prediction Campaigns

In this appendix, we discuss several practical considerations salient to the prediction campaigns and in how we disseminate the prediction information to make it useful for remote observers.

A1. Campaign Scope

The consensus fitting procedure described in Section 2.1 is iterated through all the time bins in the provided prediction datasets to provide a timeseries of source locations proceeding into the future. In a typical campaign, model results are produced on a given day using the most recent magnetogram boundary conditions available. It is therefore anticipated that the longer the time horizon of the predictions, the less accurate they will be due to future time-evolution of the boundary conditions to the model. For this reason, several updates to the predictions are issued during a typical encounter.

Additionally, since the primary goal of the predictions to produce observational targets for Earth-based observers, we are mainly concerned with times for which the predicted footpoints are "on-disk". Different Parker encounters have very different on-disk phases, with some encounters occurring mostly behind the limb, some occurring fully in view of the earth, and others (most commonly) either going behind the West limb or appearing from behind the East limb part way through the encounter. In the most recent orbits, this latter situation is almost always the case by virtue of Parker traversing more than a third of the way around the Sun during the encounter.

These considerations affect the scope of the footpoint campaign and the frequency of updates. In situations where footpoints are mostly on disk, updates are given more frequently and over a longer time interval, whereas in the converse situation, only a few updates are given and over a shorter time range. The predicted footpoints are usually truncated at the point where the footpoints go behind the Earth-facing limb, or once Parker is much further from the Sun than perihelion.

The on-disk phases are determined ahead of time via ballistic projection estimates (Badman et al., 2020) using the Parker spice kernels. Example figures and animations showing these determinations are hosted at the following url: https://sppgway.jhuapl.edu/encounters.

A2. Prediction Dissemination

In order to communicate the prediction results in a timely fashion to observers, as part of our prediction pipeline, we have defined a typical set of files produced in each update. This includes a CSV file encoding of the predicted source locations (latitude and longitude, as well as solar disk coordinates θ_x, θ_y), figures which depict the source location and uncertainty ellipse both in a Carrington/synoptic map projection and a solar disk projection, and lastly

a manually written text narrative where the consensus motion on the disk is described, and any non-trivialities are discussed.

In more recent encounters (since E12 onwards), the CSV files have included two timestamps to account for the two intervals of primary interest to making Parker-solar connections: time of arrival at Parker of plasma parcels from a given source at Parker, and the new addition of the time of emission of the source *at the footpoint* which we estimate by assuming some constant ambient solar wind speed, and constant propagation speed all the way back to the Sun. Additionally, since the solar disk rotates between these times, although the Carrington longitudes connecting both these events (emission at the source, and arrival at Parker) are fixed in time (within the assumptions of time-independent modeling), the on-disk position of the source is slightly different. Therefore a second value of (θ_x, θ_y) is provided for this earlier timestamp as well.

The emission time is subject to significant uncertainties since the true solar wind speed at Parker is unknown at the time of prediction, and moreover the solar wind accelerates so a ballistic estimate is necessarily and underestimate of the propagation time, and better constraints on it will be the subject of future work in these campaigns.

The platform over which these predictions are communicated also varies with the campaign scope. For partially on-disk orbits, with fewer updates, the predictions are conveyed over email to interested observers via a mailing list maintained by the Parker management team, while for the more involved fully on-disk occasions, campaigns are managed via the Whole Heliosphere and Planetary Interactions group who host and archive the predictions at their website: https://whpi.hao.ucar.edu/.

A3. Fitting Failures

As an operational procedure, we typically produce predictions in a relatively time-constrained manner. As such, when running the fitting procedure describe in Section 2.1 we need to be able to handle occasions when it fails. The most common failure mode we have observed is when the ensemble is bi-modal or multi-modal, which typically occurs in the vicinity of predicted HCS crossings. Another apparent failure occurs when the distribution only consists of a few points or is too clustered, in which case the fitting software we use (Fraenkel, 2014) has numerical difficulties, and a fit does not converge.

In the first case, we typically find the different peaks in the ensemble are located at very different latitudes. As a solution, we therefore take the most probable peak (the peak which contains the most ensemble members) and exclude the other from the fit via masking by latitude. When reporting the predictions, although our consensus data sets show this primary peak, we usually mention the coronal feature corresponding to the other peaks in the text narrative.

In the second case where the ensemble is too tightly clustered, the purpose of the Kent distribution in capturing the uncertainty is less necessary since we can simply regard the uncertainty as "small". Therefore when this fitting failure mode occurs we do not attempt to fit again but instead, simply take the median longitude and latitude from the ensemble and use this as the consensus location for that time window.

Data Availability Statement

The predicted footpoint ensembles used in Figures 2, 3, 5 and 6 are hosted in a GitHub repository accompanying this paper (Badman et al., 2023), which also contains a python jupyter notebook which reproduces all the figures shown in this paper and includes the analysis steps of producing the consensus footpoints.

Datasets

All data other than the footpoint ensembles are publicly available from the relevant NASA, mission or instrument webpages, and their access is performed inline by the aforementioned jupyter notebook.
The Parker Solar Probe FIELDS (Bale et al., 2016; Pulupa et al., 2017) and SWEAP (Kasper et al., 2016; Livi et al., 2022) data used for in the study to constrain and validate the footpoint predictions are archived at the Space Physics Data Facility via https://spdf.gsfc.nasa.gov/pub/data/psp/ and are publicly available (Candey, 2021). These data are accessed programmatically in this work in python by pyspedas (see below).
The Solar Dynamics Observatory Atmospheric Imager Assembly data (Lemen et al., 2012) used to contextualize footpoint measurements in this work are archived by the Virtual Solar Observatory https://nso.edu/data/vso/, and

the Joint Science Operations Center http://jsoc.stanford.edu/ and are publicly available. These data are accessed programmatically in this work in python via solarsynoptic (see below).

The ADAPT magnetic field maps (C. N. Arge et al., 2010; Arge et al., 2011, 2013; Hickmann et al., 2015) used to run coronal models in this work are archived by the National Solar Observatory at https://gong.nso.edu/adapt/ and are publicly available. Data is accessed directly in this work via requests at the above URL.

Software

All software used in this paper are either included as helper functions in the linked repository (Badman et al., 2023) or use open source python libraries:

Version 5.1 of the astropy is used throughout this work for coordinate and frame transformations and working with units. It is preserved at doi:10.5281/zenodo.6579729, available via open access and developed openly at https://github.com/astropy/astropy (Astropy Collaboration et al., 2013, 2018, 2022).

Version 0.2.0 of the astrospice is used throughout this work for spacecraft trajectory calculation. The persistent link is https://pypi.org/project/astrospice/0.2.0/. It is developed openly at https://github.com/astrospice/astrospice.

Version 4.3.5 of func_timeout is used for error handling in the consensus fitting procedure. The persistent link is https://pypi.org/project/func-timeout/4.3.5/. It is developed openly at https://github.com/kata198/func_timeout.

kent_distribution is used for establishing consensus fits in this work. It is openly developed at https://github.com/edfraenkel/kent_distribution (Fraenkel, 2014). An edited version of this repository as used here to allow it to function in python3 is available via Badman et al. (2023).

Version 3.5.2 of matplotlib is used for all figures presented in this work. It is preserved at doi:10.5281/zenodo.6513224, available via open access and developed openly at https://github.com/matplotlib/matplotlib (Hunter, 2007).

Version 1.1.2 of pfsspy is used for PFSS coronal modeling and field line tracing throughout this work. It is preserved at doi:10.5281/zenodo.7025396, available via open access and developed openly at https://github.com/dstansby/pfsspy (Stansby et al., 2020).

Version 1.4.18 of pyspedas is used for PSP data access. The persistent link is https://pypi.org/project/pyspedas/1.4.18/. The project is developed openly at https://github.com/spedas/pyspedas (Angelopoulos et al., 2019).

Version 1.9.1 of scipy is used for data interpolation in this work. It is preserved at doi:10.5281/zenodo.7026742, available via open access and developed openly at https://github.com/scipy/scipy (Virtanen et al., 2020).

Version 5.1.2 of spiceypy is the engine behind astrospice. It is preserved at doi:10.5281/zenodo.7204403 and is available via open access and developed openly at https://github.com/AndrewAnnex/SpiceyPy (Annex et al., 2020).

Version 4.1.0 sunpy is used for enumerable tasks in this manuscript, most notably frame transformations, plotting and doing world to pixel coordinate conversions. It is preserved at doi:10.5281/zenodo.7314636 and is available via open access and developed openly at https://github.com/sunpy/sunpy (The SunPy Community et al., 2020).

Acknowledgments

Parkar was designed, built, and is now operated by the Johns Hopkins Applied Physics Laboratory as part of NASA's Living with a Star (LWS) program (contract NNN06AA01C). Support from the LWS management and technical team has played a critical role in the success of the PSP mission. The FIELDS and SWEAP experiments on the Parker Solar Probe spacecraft were designed and developed under NASA contract NNN06AA01C.

The ADAPT model development is supported by Air Force Research Laboratory (AFRL), along with AFOSR (Air Force Office of Scientific Research) tasks 18RVCOR126 and 22RVCOR012. This work utilizes data produced collaboratively between AFRL and the National Solar Observatory (NSO). The views expressed are those of the authors and do not reflect the official guidance or position of the United States Government, the Department of Defense (DoD) or of the United States Air Force. The appearance of external hyperlinks does not constitute endorsement by the DoD of the linked websites, or the information, products, or services contained therein. The DoD does not exercise any editorial, security, or other control over the information you may find at these locations.

The authors thank the Whole Heliosphere and Planetary Interactions group who coordinated the first iteration of the now-regular footpoint predictions presented in this work and have regularly supported the dissemination and hosting of the results to remote observers.

RCA acknowledges support from NASA Grant 80NSSC22K0993.

PR gratefully acknowledges support from NASA (80NSSC18K0100, NNX16AG86 G, 80NSSC18K1129, 80NSSC18K0101, 80NSSC20K1285, and NNN06AA01C), NOAA (NA18NWS4680081), and the U.S. Air Force (FA9550-15-C-0001).

STB thanks Carlos Braga for useful discussions on the CME leg crossing studied in McComas et al. (2023) which coincides with the first sub-alfvènic interval in this work.

JLV acknowledges support from NASA PSP-GI 80NSSC23K0208.

TKK and NVP acknowledge support from NASA Grant 80NSSC20K1453, NSF/NASA SWQU Grant 2028154, and the PSP mission through the UAH–SAO agreement SV4-84017. TKK acknowledges support from AFOSR grant FA9550-19-1-0027.

References

Altschuler, M. D., & Newkirk, G. (1969). Magnetic fields and the structure of the solar corona. I: Methods of calculating coronal fields. *Solar Physics*, *9*(1), 131–149. https://doi.org/10.1007/BF00145734

Angelopoulos, V., Cruce, P., Drozdov, A., Grimes, E. W., Hatzigeorgiu, N., King, D. A., et al. (2019). The space physics environment data analysis system (SPEDAS). *SSRv*, *215*(1), 9. https://doi.org/10.1007/s11214-018-0576-4

Annex, A., Pearson, B., Seignovert, B., Carcich, B., Eichhorn, H., Mapel, J., et al. (2020). SpiceyPy: A pythonic wrapper for the SPICE. *Journal of Open Source Software*, *5*(46), 2050. https://doi.org/10.21105/joss.02050.toolkit

Antiochos, S. K., Mikić, Z., Titov, V. S., Lionello, R., & Linker, J. A. (2011). A model for the sources of the slow solar wind. *The Astrophysical Journal*, *731*(2), 112. https://doi.org/10.1088/0004-637X/731/2/112

Arge, C., Luhmann, J., Odstrcil, D., Schrijver, C., & Li, Y. (2004). Stream structure and coronal sources of the solar wind during the May 12th, 1997 CME. *Journal of Atmospheric and Solar-Terrestrial Physics*, *66*(15), 1295–1309. https://doi.org/10.1016/j.jastp.2004.03.018

Arge, C. N., Henney, C. J., Hernandez, I. G., Toussaint, W. A., Koller, J., & Godinez, H. C. (2013). Modeling the corona and solar wind using ADAPT maps that include far-side observations, In *Solar wind 13 (vol. CS-1539* (pp. 11–14). American Institute of Physics. https://doi.org/10.1063/1.4810977

Arge, C. N., Henney, C. J., Koller, J., Compeau, C. R., Young, S., MacKenzie, D., et al. (2010). Air force data assimilative photospheric flux transport (adapt) model. *AIP Conference Proceedings*, *1216*(1), 343–346. https://doi.org/10.1063/1.3395870

Arge, C. N., Henney, C. J., Koller, J., Toussaint, W. A., Harvey, J. W., & Young, S. (2011). Improving data drivers for coronal and solar wind models. In N. V. Pogorelov, E. Audit, & G. P. Zank (Eds.), *Journal of physics* (Vol. CS-444, p. 99). Astronomical Society of the Pacific.

Arge, C. N., Odstrcil, D., Pizzo, V. J., & Mayer, L. R. (2003). Improved method for specifying solar wind speed near the sun. *AIP Conference Proceedings*, *679*(1), 190–193. https://doi.org/10.1063/1.1618574

Arge, C. N., & Pizzo, V. J. (2000). Improvement in the prediction of solar wind conditions using near-real time solar magnetic field updates. *Journal of Geophysical Research*, *105*(A5), 10465–10479. https://doi.org/10.1029/1999ja000262

Astropy Collaboration, Price-Whelan, A. M., Lim, P. L., Earl, N., Starkman, N., Bradley, L., et al. (2022). The astropy project: Sustaining and growing a community-oriented open-source project and the latest major release (v5.0) of the core package. *The Astrophysical Journal*, *935*(2), 167. https://doi.org/10.3847/1538-4357/ac7c74

Badman, S. T., Bale, S. D., Martínez Oliveros, J. C., Panasenco, O., Velli, M., Stansby, D., et al. (2020). Magnetic connectivity of the ecliptic plane within 0.5 au: Potential field source surface modeling of the first parker solar probe encounter. *Astrophysical Journal Supplement Series*, *246*(2), 23. https://doi.org/10.3847/1538-4365/ab4da7

Badman, S. T., Bale, S. D., Rouillard, A. P., Bowen, T. A., Bonnell, J. W., Goetz, K., et al. (2021). Measurement of the open magnetic flux in the inner heliosphere down to 0.13 AU. *Astronomy & Astrophysics*, *650*, A18. https://doi.org/10.1051/0004-6361/202039407

Badman, S. T., Brooks, D. H., Poirier, N., Warren, H. P., Petrie, G., Rouillard, A. P., et al. (2022). Constraining global coronal models with multiple independent observables. *The Astrophysical Journal*, *932*(2), 135. https://doi.org/10.3847/1538-4357/ac6610

Badman, S. T., Riley, P., Jones, S. I., Kim, T., Allen, R. C., Arge, C. N., et al. (2023). PSP-E10-sources - Python repository to reproduce figures in badman+ "prediction and verification of parker solar probe solar wind sources at 13.3r⊙". *Zenodo*. https://doi.org/10.5281/zenodo.7590078

Bale, S. D., Badman, S. T., Bonnell, J. W., Bowen, T. A., Burgess, D., Case, A. W., et al. (2019). Highly structured slow solar wind emerging from an equatorial coronal hole. *Nature*, *576*(7786), 237–242. https://doi.org/10.1038/s41586-019-1818-7

Bale, S. D., Drake, J. F., McManus, M. D., Desai, M. I., Badman, S. T., Larson, D. E., et al. (2023). Interchange reconnection as the source of the fast solar wind within coronal holes. *Nature*. https://doi.org/10.48550/ARXIV.2208.07932

Bale, S. D., Goetz, K., Harvey, P. R., Turin, P., Bonnell, J. W., Dudok de Wit, T., et al. (2016). The FIELDS instrument suite for solar probe plus. Measuring the coronal plasma and magnetic field, plasma waves and turbulence, and Radio signatures of solar transients. *SSRv*, *204*(1–4), 49–82. https://doi.org/10.1007/s11214-016-0244-5

Candey, R. (2021). NASA space physics data facility archives and the heliophysics data environment and international heliophysics data alliance. In 43rd COSPAR scientific assembly (Vol. *43*, p. 2387). Held 28 January - 4 February.

Caplan, R. M., Downs, C., Linker, J. A., & Mikic, Z. (2021). Variations in finite-difference potential fields. *Acta Pathologica Japonica*, *915*(1), 44. https://doi.org/10.3847/1538-4357/abfd2f

Carrington, R. C. (1863). Observations of the spots on the Sun: From November 9, 1853, to March 24, 1861, made at Redhill.

Chhiber, R., Matthaeus, W. H., Cohen, C. M. S., Ruffolo, D., Sonsrettee, W., Tooprakai, P., et al. (2021). Magnetic field line random walk and solar energetic particle path lengths. Stochastic theory and PSP/IS⊙IS observations. *Astronomy & Astrophysics*, *650*, A26. https://doi.org/10.1051/0004-6361/202039816

Chhiber, R., Matthaeus, W. H., Usmanov, A. V., Bandyopadhyay, R., & Goldstein, M. L. (2022). An extended and fragmented Alfvén zone in the young solar wind. *Monthly Notices of the Royal Astronomical Society*, *513*(1), 159–167. https://doi.org/10.1093/mnras/stac779

Dakeyo, J.-B., Maksimovic, M., Démoulin, P., Halekas, J., & Stevens, M. L. (2022). Statistical analysis of the radial evolution of the solar winds between 0.1 and 1 au and their semiempirical isopoly fluid modeling. *The Astrophysical Journal*, *940*(2), 130. https://doi.org/10.3847/1538-4357/ac9b14

Da Silva, D., Arge, C., & Jones, S. (2022). Predicting solar wind footpoints as probability distributions using WSA/ADAPT. *The Third Triennial Earth-Sun Summit*, *54*, 2022n7i109p03.

Davis, N., Chandran, B. D. G., Bowen, T. A., Badman, S. T., Dudok de Wit, T., Chen, C. H. K., et al. (2023). The evolution of the 1/f range within a single fast-solar-wind stream between 17.4 and 45.7 solar Radii. arXiv e-prints, arXiv:2303. 01663. https://doi.org/10.48550/arXiv.2303.01663

DeForest, C. E., Howard, T. A., & McComas, D. J. (2014). Inbound waves in the solar corona: A direct indicator of Alfvén surface location. *The Astrophysical Journal*, *787*(2), 124. https://doi.org/10.1088/0004-637X/787/2/124

De Pontieu, B., Title, A. M., Lemen, J. R., Kushner, G. D., Akin, D. J., Allard, B., et al. (2014). The interface region imaging spectrograph (IRIS). *Solar Physics*, *289*(7), 2733–2779. https://doi.org/10.1007/s11207-014-0485-y

Fox, N. J., Velli, M. C., Bale, S. D., Decker, R., Driesman, A., Howard, R. A., et al. (2016). The solar probe Plus mission: Humanity's first visit to our star. *SSRv*, *204*(1–4), 7–48. https://doi.org/10.1007/s11214-015-0211-6

Fraenkel, E. D. (2014). *From radio pulse to elusive particle (Unpublished doctoral dissertation)*. University of Groningen.

Halekas, J. S., Whittlesey, P., Larson, D. E., Maksimovic, M., Livi, R., Berthomier, M., et al. (2022). The radial evolution of the solar wind as organized by electron distribution parameters. *The Astrophysical Journal*, *936*(1), 53. https://doi.org/10.3847/1538-4357/ac85b8

Hickmann, K. S., Godinez, H. C., Henney, C. J., & Arge, C. N. (2015). Data assimilation in the ADAPT photospheric flux transport model. *Solar Physics*, *290*(4), 1105–1118. https://doi.org/10.1007/s11207-015-0666-3

Hunter, J. D. (2007). Matplotlib: A 2D graphics environment. *Computing in Science & Engineering*, *9*(3), 90–95. https://doi.org/10.1109/MCSE.2007.55

Kasper, J. C., Abiad, R., Austin, G., Balat-Pichelin, M., Bale, S. D., Belcher, J. W., et al. (2016). Solar wind electrons alphas and protons (SWEAP) investigation: Design of the solar wind and coronal plasma instrument suite for solar probe plus. *SSRv*, *204*(1–4), 131–186. https://doi.org/10.1007/s11214-015-0206-3

Kasper, J. C., Klein, K. G., Lichko, E., Huang, J., Chen, C. H. K., Badman, S. T., et al. (2021). Parker solar probe enters the magnetically dominated solar corona. *Physical Review Letters*, *127*(25), 255101. https://doi.org/10.1103/PhysRevLett.127.255101

Kent, J. T. (1982). The Fisher-Bingham distribution on the sphere. *Journal of the Royal Statistical Society: Series B*, *44*(1), 71–80. https://doi.org/10.1111/j.2517-6161.1982.tb01189.x. Retrieved 2023-01-10, from http://www.jstor.org/stable/2984712

Kim, T. K., Pogorelov, N. V., Arge, C. N., Henney, C. J., Jones-Mecholsky, S. I., Smith, W. P., et al. (2020). Predicting the solar wind at the parker solar probe using an empirically driven MHD model. *The Astrophysical Journal Supplement*, *246*(2), 40. https://doi.org/10.3847/1538-4365/ab58c9

Kinnison, J., Vaughan, R., Hill, P., Raouafi, N., Guo, Y., & Pinkine, N. (2020). Parker solar probe: A mission to touch the sun. In *2020 ieee aerospace conference* (pp. 1–14). https://doi.org/10.1109/AERO47225.2020.9172703

Koukras, A., Dolla, L., & Keppens, R. (2022). Estimating uncertainties in the back-mapping of the fast solar wind. *arXiv e-prints*. arXiv:2212.11553.

Lemen, J. R., Title, A. M., Akin, D. J., Boerner, P. F., Chou, C., Drake, J. F., et al. (2012). The atmospheric imaging assembly (AIA) on the solar dynamics observatory (SDO). *Solar Physics*, *275*(1), 17–40. https://doi.org/10.1007/s11207-011-9776-8

Liu, Y. D., Chen, C., Stevens, M. L., & Liu, M. (2021). Determination of solar wind angular momentum and Alfvén radius from parker solar probe observations. *The Astrophysical Journal Letters*, *908*(2), L41. https://doi.org/10.3847/2041-8213/abe38e

Liu, Y. D., Ran, H., Hu, H., & Bale, S. D. (2023). On the generation and evolution of Switchbacks and the morphology of alfvénic transition: Low mach-number boundary layers. arXiv e-prints, arXiv:2301.05829.

Livi, R., Larson, D. E., Kasper, J. C., Abiad, R., Case, A. W., Klein, K. G., et al. (2022). The solar probe ANalyzer-ions on the parker solar probe. *Acta Pathologica Japonica*, *938*(2), 138. https://doi.org/10.3847/1538-4357/ac93f5

MacNeil, A. R., Owens, M. J., Finley, A. J., & Matt, S. P. (2021). A statistical evaluation of ballistic backmapping for the slow solar wind: The interplay of solar wind acceleration and corotation. *Monthly Notices of the Royal Astronomical Society*. https://doi.org/10.1093/mnras/stab2965

McComas, D. J., Alexander, N., Angold, N., Bale, S., Beebe, C., Birdwell, B., et al. (2016). Integrated science investigation of the sun (ISIS): Design of the energetic particle investigation. *SSRv*, *204*(1–4), 187–256. https://doi.org/10.1007/s11214-014-0059-1

McComas, D. J., Sharma, T., Christian, E. R., Cohen, C. M. S., Desai, M. I., Hill, M. E., et al. (2023). Parker solar probe encounters the leg of a coronal mass ejection at 14 solar radii. *The Astrophysical Journal*, *943*(2), 71. https://doi.org/10.3847/1538-4357/acab5e

Moncuquet, M., Meyer-Vernet, N., Issautier, K., Pulupa, M., Bonnell, J. W., Bale, S. D., et al. (2020). First *in* situ measurements of electron density and temperature from quasi-thermal noise spectroscopy with parker solar probe/FIELDS. *ApJS*, *246*(2), 44. https://doi.org/10.3847/1538-4365/ab5a84

Müller, D., St. Cyr, O. C., Zouganelis, I., Gilbert, H. R., Marsden, R., Nieves-Chinchilla, T., et al. (2020). The solar orbiter mission. Science overview. *Astronomy & Astrophysics*, *642*, A1. https://doi.org/10.1051/0004-6361/202038467

Neugebauer, M., Forsyth, R. J., Galvin, A. B., Harvey, K. L., Hoeksema, J. T., Lazarus, A. J., et al. (1998). 7 Spatial structure of the solar wind and comparisons with solar data and models. *Journal of Geophysical Research*, *103*(A7), 14587–14599. https://doi.org/10.1029/98JA00798

Nolte, J. T., Krieger, A. S., Timothy, A. F., Gold, R. E., Roelof, E. C., Vaiana, G., et al. (1976). Coronal holes as sources of solar wind. *Solar Physics*, *46*(2), 303–322. https://doi.org/10.1007/BF00149859

Nolte, J. T., & Roelof, E. C. (1973). Large-scale structure of the interplanetary medium, I: High coronal source longitude of the quiet-time solar wind. *Solar Physics*, *33*(1), 241–257. https://doi.org/10.1007/BF00152395

Panasenco, O., Velli, M., D'Amicis, R., Shi, C., Réville, V., Bale, S. D., et al. (2020). Exploring solar wind origins and connecting plasma flows from the parker solar probe to 1 au: Nonspherical source surface and Alfvénic fluctuations. *The Astrophysical Journal - Supplement Series*, *246*(2), 54. https://doi.org/10.3847/1538-4365/ab61f4

Parker, E. N. (1958). Dynamics of the interplanetary gas and magnetic fields. *The Astrophysical Journal*, *128*, 664. https://doi.org/10.1086/146579

Pogorelov, N. V. (2023). Heliosphere in the local interstellar medium, Proceedings of IAU. In D. Bisikalo, D. Wiebe, & C. Boily (Eds.), *The predictive power of computational astrophysics as a discovery tool* (Vol. 16, pp. 309–323). https://doi.org/10.1017/S1743921322001612

Pogorelov, N. V., Borovikov, S., Heerikhuisen, J., Kim, T., Kryukov, I., & Zank, G. (2014). Ms-flukss and its application to modeling flows of partially ionized plasma in the heliosphere. In *Proceedings of the 2014 annual conference on extreme science and engineering discovery environment*. Association for Computing Machinery. https://doi.org/10.1145/2616498.2616499

Price-Whelan, A. M., Price-Whelan, A. M., Sipőcz, B. M., Günther, H. M., Lim, P. L., Crawford, S. M., et al. (2018). The astropy project: Building an open-science project and status of the v2.0 core package. *The Astronomical Journal*, *156*(3), 123. https://doi.org/10.3847/1538-3881/aabc4f

Pulupa, M., Bale, S. D., Bonnell, J. W., Bowen, T. A., Carruth, N., Goetz, K., et al. (2017). The solar probe plus radio frequency Spectrometer: Measurement requirements, analog design, and digital signal processing. *Journal of Geophysical Research (Space Physics)*, *122*(3), 2836–2854. https://doi.org/10.1002/2016JA023345

Riley, P., Downs, C., Linker, J. A., Mikic, Z., Lionello, R., & Caplan, R. M. (2019). Predicting the structure of the solar corona and inner heliosphere during parker solar probe's first perihelion pass. *The Astrophysical Journal*, *874*(2), L15. https://doi.org/10.3847/2041-8213/ab0ec3

Riley, P., Linker, J. A., & Mikić, Z. (2001). An empirically-driven global MHD model of the solar corona and inner heliosphere. *Journal of Geophysical Research*, *106*(A8), 15889–15901. https://doi.org/10.1029/2000JA000121

Riley, P., Linker, J. A., Mikić, Z., Lionello, R., Ledvina, S. A., & Luhmann, J. G. (2006). A comparison between global solar magnetohydrodynamic and potential field source surface model results. *The Astrophysical Journal*, *653*(2), 1510–1516. https://doi.org/10.1086/508565

Riley, P., Lionello, R., Caplan, R. M., Downs, C., Linker, J. A., Badman, S. T., & Stevens, M. L. (2021). Using parker solar probe observations during the first four perihelia to constrain global magnetohydrodynamic models. *Astronomy & Astrophysics*, *650*, A19. https://doi.org/10.1051/0004-6361/202039815

Rimmele, T. R., Warner, M., Keil, S. L., Goode, P. R., Knölker, M., Kuhn, J. R., et al. (2020). The Daniel K. Inouye solar telescope - Observatory overview. *Solar Physics*, *295*(12), 172. https://doi.org/10.1007/s11207-020-01736-7

Robitaille, T. P., Robitaille, T. P., Tollerud, E. J., Greenfield, P., Droettboom, M., Bray, E., et al. (2013). Astropy: A community Python package for astronomy. *Astronomy & Astrophysics*, *558*, A33. https://doi.org/10.1051/0004-6361/201322068

Rochus, P., Auchère, F., Berghmans, D., Harra, L., Schmutz, W., Schühle, U., et al. (2020). The solar orbiter EUI instrument: The extreme ultraviolet imager. *Astronomy & Astrophysics*, *642*, A8. https://doi.org/10.1051/0004-6361/201936663

Rouillard, A. P., Pinto, R. F., Vourlidas, A., De Groof, A., Thompson, W. T., Bemporad, A., et al. (2020). Models and data analysis tools for the Solar Orbiter mission. *Astronomy & Astrophysics*, *642*, A2. https://doi.org/10.1051/0004-6361/201935305

Schatten, K. H. (1972). In *Current sheet magnetic model for the solar Corona. In C. P. Sonett, P. J. Coleman, & J. M. Wilcox (Eds.), Solar wind. edited by Scientific and technical information office, national aeronautics and space administration* (Vol. 308, p. 44).

Schatten, K. H., Wilcox, J. M., & Ness, N. F. (1969). A model of interplanetary and coronal magnetic fields. *Solar Physics*, *6*(3), 442–455. https://doi.org/10.1007/BF00146478

Singh, T., Kim, T. K., Pogorelov, N. V., & Arge, C. N. (2022). Ensemble simulations of the 2012 July 12 coronal mass ejection with the constant-turn flux rope model. *The Astrophysical Journal*, *933*(2), 123. https://doi.org/10.3847/1538-4357/ac73f3

Stansby, D., Horbury, T. S., Wallace, S., & Arge, C. N. (2019). Predicting large-scale coronal structure for parker solar probe using open source software. *Research Notes of the AAS*, *3*(3), 57. https://doi.org/10.3847/2515-5172/ab13b7

Stansby, D., & Verscharen, D. (2022). Test problems for potential field source surface extrapolations of solar and stellar magnetic fields. arXiv e-prints, arXiv:2201.07783.

Stansby, D., Yeates, A., & Badman, S. (2020). pfsspy: A Python package for potential field source surface modelling. *Journal of Open Source Software*, *5*(54), 2732. https://doi.org/10.21105/joss.02732

The SunPy Community, Barnes, W. T., Barnes, W. T., Bobra, M. G., Christe, S. D., Freij, N., et al. (2020). The sunpy project: Open source development and status of the version 1.0 core package. *The Astrophysical Journal*, *890*(1), 68. https://doi.org/10.3847/1538-4357/ab4f7a

Van der Holst, B., Manchester, I. W. B., Klein, K. G., & Kasper, J. C. (2019). Predictions for the first parker solar probe encounter. *The Astrophysical Journal Letters*, *872*(2), L18. https://doi.org/10.3847/2041-8213/ab04a5

Verscharen, D., Bale, S. D., & Velli, M. (2021). Flux conservation, radial scalings, mach numbers, and critical distances in the solar wind: Magnetohydrodynamics and Ulysses observations. *Monthly Notices of the Royal Astronomical Society*, *506*(4), 4993–5004. https://doi.org/10.1093/mnras/stab2051

Virtanen, P., Gommers, R., Oliphant, T. E., Haberland, M., Reddy, T., Cournapeau, D., et al. (2020). SciPy 1.0 contributors (2020). SciPy 1.0: Fundamental algorithms for scientific computing in Python. *Nature Methods*, *17*(3), 261–272. https://doi.org/10.1038/s41592-019-0686-2

Vourlidas, A., Howard, R. A., Plunkett, S. P., Korendyke, C. M., Thernisien, A. F. R., Wang, D., et al. (2016). The wide-field imager for solar probe plus (WISPR). *SSRv*, *204*(1–4), 83–130. https://doi.org/10.1007/s11214-014-0114-y

Wallace, S., Jones, S. I., Arge, C. N., Viall, N. M., & Henney, C. J. (2022). New insights into the first two PSP solar encounters enabled by modeling analysis with ADAPT-WSA. *The Astrophysical Journal*, *935*(1), 24. https://doi.org/10.3847/1538-4357/ac731c

Wang, Y. M., Grappin, R., Robbrecht, E., & Sheeley, N. R. J. (2012). On the nature of the solar wind from coronal pseudostreamers. *The Astrophysical Journal*, *749*(2), 182. https://doi.org/10.1088/0004-637X/749/2/182

Wang, Y.-M., & Ko, Y.-K. (2019). Observations of slow solar wind from equatorial coronal holes. *The Astrophysical Journal*, *880*(2), 146. https://doi.org/10.3847/1538-4357/ab2add

Wang, Y. M., & Panasenco, O. (2019). Observations of solar wind from Earth-directed coronal pseudostreamers. *The Astrophysical Journal*, *872*(2), 139. https://doi.org/10.3847/1538-4357/aaff5e

Wang, Y.-M., & Sheeley, N. R., Jr. (1990). Solar wind speed and coronal flux-tube expansion. *Acta Pathologica Japonica*, *355*, 726–732. https://doi.org/10.1086/168805

Weber, E. J., Davis, J., & Leverett, A. (1967). The angular momentum of the solar wind. *The Astrophysical Journal*, *148*, 217–227. https://doi.org/10.1086/149138

Wexler, D. B., Stevens, M. L., Case, A. W., & Song, P. (2021). Alfvén speed transition zone in the solar corona. *The Astrophysical Journal Letters*, *919*(2), L33. https://doi.org/10.3847/2041-8213/ac25fa

Zhao, L. L., Zank, G. P., Adhikari, L., Telloni, D., Stevens, M., Kasper, J. C., et al. (2022). Turbulence and waves in the sub-alfvénic solar wind observed by the parker solar probe during encounter 10. *The Astrophysical Journal Letters*, *934*(2), L36. https://doi.org/10.3847/2041-8213/ac8353